PERGAMON

International Journal of Multiphase Flow 25 (1999) 1321–1372

International Journal of Multiphase Flow

www.elsevier.com/locate/ijmulflow

Lateral forces on spheres in turbulent uniform shear flow

F.J. Moraga [1], F.J. Bonetto, R.T. Lahey*

Center for Multiphase Research, Rensselaer Polytechnic Institute, Troy, NY 12180-3590, USA

Received 10 August 1998; received in revised form 29 April 1999

It is our pleasure to have an opportunity to honor Professor Gad Hetsroni. His vision and leadership in establishing the *International Journal of Multiphase Flow* has dramatically advanced the field

Abstract

The lateral force on a tethered rigid sphere submerged in a turbulent, uniform shear flow of water was measured. Periodic and non-periodic motions of the sphere were observed depending on flowrate, shear and sphere density. The direction of the observed lateral force was opposite to that predicted by inviscid theory and increased in magnitude as the sphere's Reynolds numbers based on relative velocity, Re, and average shear, Re_∇, increased. The lateral force was found to correlate with the product $Re\,Re_\nabla$. The data suggests that a sign reversal occurs at relatively small values of the product $Re\,Re_\nabla$, where the lateral force is dominated by inviscid effects. The results are explained assuming that the lateral forces on rigid spheres are a consequence of two competing factors: namely, inviscid lift forces and the vortex shedding-induced lateral forces which are dominant for higher Reynolds numbers. An estimate of the kinetic energy in the wake was used to show that the vortex shedding-induced lateral forces correlate with the product Re Re_∇ and are in a direction opposite to the inviscid lift force. Combining the experimental data of this study with similar data a correlation for the lift coefficient of spheres in turbulent shear flows was developed. This correlation is applicable to turbulent multiphase flows having a spherical dispersed phase.

Keywords: Lift force; Vortex shedding; Wake; Sphere; Shear; Two-fluid model

* Corresponding author.
E-mail address: laheyr@rpi.edu (R.T. Lahey)
[1] Currently at Oak Ridge Associated Universities, Oak Ridge, TN, USA.

0301-9322/99/$ - see front matter
PII: S0301-9322(99)00045-2

1. Introduction

Multiphase turbulent flows in which dispersed particles are transported by a continuous phase are encountered in many industrial, environmental and naval applications. A multidimensional two-fluid model has been developed (Alajbegović, 1994; Lahey et al., 1993) in order to achieve prediction capabilities which are accurate enough to design equipment and predict two-phase flows. The need to limit the amount of information handled by this mechanistic model has lead to the introduction of averaged equations which are similar to those used for single-phase turbulent flows. Unfortunately, ensemble averaging leads to a loss of information, which has to be explicitly put back into the equations through modeling of the more important physical phenomena (i.e., the closure process). Physical insight is needed to identify the phenomena that are of relevance for each particular flow. This fact is particularly true for interfacial forces, which are instrumental in the determination of the dispersed phase's distribution profiles. From studies of bubbly, fully developed flow in a vertical pipe of circular (Wang, 1986; Wang et al., 1986) and non-circular cross-sections (Lopez de Bertonado, 1991; Lahey et al., 1993) it has been shown that the discrete phase's distribution profile arises from a balance of the lateral forces and turbulent dispersion.

In current versions of the two-fluid model (e.g., Alajbegović, 1994; Bel Fdhila, 1991; Grossetete, 1995) the lateral forces on a dispersed particle submerged in a shear flow are modeled assuming inviscid flow around a rigid sphere. Drew and Lahey (1987, 1990) and Auton (1987) independently derived the lateral lift force on a sphere as:

$$F_{\mathrm{L(inviscid)}} = C_{\mathrm{L}}\rho V\omega \times v_{\mathrm{r}} \tag{1}$$

where V is the volume of the sphere, ρ is the fluid density, v_{r} and ω are the relative velocity of the sphere with respect to the liquid and the average vorticity at the sphere's centroid, respectively. Drew and Lahey and Auton's analysis yield $C_{\mathrm{L}} = 0.5$ for a sphere. It must be stressed that since the calculation was based on inviscid flow, wake effects were not taken into account.

For fully developed flow in a vertical pipe the experimental data yield $0.01 < C_{\mathrm{L}} < 0.15$ with $C_{\mathrm{L}} = 0.1$ fitting most of the data (Wang et al., 1986; Lahey et al., 1993). It should be stressed that to date, C_{L} has been considered a constant independent of the local relative velocity, average vorticity and particle diameter. This hypothesis was used because of lack of experimental or theoretical work to enable the quantification of C_{L} as a function of the above-mentioned variables. The inability to solve all the details of the flow require that v_{r} and ω be evaluated using the time-averaged values of the corresponding instantaneous magnitudes. In practice, however, the lateral force experienced by a particle will depend on the instantaneous velocity field around it rather than the average magnitudes. Thus, the motion of some bubbles may depart significantly from that predicted by Eq. (1). This fact makes Eq. (1) valid only when enough statistics are acquired and averaged. Indeed, the values of C_{L} successfully fitted to experimental data are the result of ensemble-averaging.

The works of several authors have proved the importance of this ensemble-averaging. Lance et al. (1991) were not able to observe a lateral migration in bubbles moving through a uniform turbulent shear flow of water ($\omega = 2.9\ \mathrm{s}^{-1}$), although Eq. (1) predicted a lateral migration of 8 mm at the end of the bubble trajectory through the shear flow. More recently, Ford and Loth

(1997), Taeibi-Rahni and Loth (1996) and Loth et al. (1997) have proved, through numerical simulations and experiments, that the trajectories of individual bubbles can differ considerably from the predicted using Eq. (1).

Despite its success for fully developed vertical flow in a pipe the two-fluid model has yet to be successfully extended to some other conduit flow geometries. In particular, Bel Fdhila (1991) showed that in order to fit his experimental data of bubbly flow in a vertical pipe having a sudden expansion, the lift coefficient, C_L, would have to be negative. This result agrees qualitatively with the measurements of Rinne and Loth (1995, 1996). Also, Aloui and Souhar (1996a, 1996b) found a qualitatively different void fraction distribution for horizontal air/water bubbly flow in a flat symmetric duct of rectangular cross-section undergoing a sudden expansion. The cause of the differences between the void fraction distributions for vertical axisymmetric (Bel Fdhila, 1991; Rinne and Loth, 1995, 1996) and horizontal rectangular sudden expansions (Aloui and Souhar, 1996a, 1996b) has yet to be identified. Grossetete (1995) applied the two-fluid model to developing bubbly flow in a vertical pipe. He found that for some injection conditions the lift coefficient would have to be negative in order to fit the experimental data.

Many possible explanations of the sign reversal of the lift force have been explored. Perhaps the most obvious possibility for bubbly flows is bubble deformation. Serizawa and Kataoka (1987) and Žun (1985) found evidence that bubble size and shape affect the discrete phase's distribution profile and plays a role in the transition from bubbly to slug flow. Kariyasaki (1987) used a novel experimental technique to measure the lift on bubbles, drops and rigid particles for low Reynolds numbers ($Re<1$) and found that bubbles move in an opposite direction to rigid particles. His results suggest that deformation plays a key role in determining the magnitude and the direction of the lift. Indeed, Kariyasaki attributed the change in sign to the fact that bubbles adopted an airfoil shape which was responsible for the observed aerodynamical lift. The airfoil shape found by Kariyasaki results from an equilibrium between tangential stresses and surface tension. Other researchers, Ervin and Tryggvason, 1994; Tomiyama et al., 1993, 1995; Tagaki and Matsumoto, 1995, obtained similar results for the sign of the lift force and the shape of bubbles using direct numerical simulation. However, the need to keep track of a moving interface and the large CPU times required prevented these researchers from producing general and consistently proven correlations for the lift force for the different non-dimensional numbers involved. Moreover, the numerical simulations cited above were limited to low Reynolds numbers, $Re<50$ (based on bubble size), and thus do not cover the range of Reynolds number of interest in most bubbly flow applications ($Re \simeq 1000$).

Alajbegović et al., (1994) suggested that rotation of solid spheres under the influence of shear could reduce the magnitude of the lift coefficient and explain his results for solid/fluid fully developed flow in a vertical pipe. Significantly, Taneda (1957), Davies (1949) and Maccoll (1928) found evidence that solid particle rotation induces wake asymmetries, which, in turn, may reverse the sign of lateral forces. Viets (1971) showed that an accelerating sphere in an axisymmetric flow is subjected to a lift force due to vortex shedding instabilities. This mechanism could produce an unsteady lift force in a sudden expansion, a jet, or any other geometry where particles are subjected to acceleration. Wake phenomena are particularly important when the ratio of the discrete to continuous phase densities is small, as in bubbly

flows, because, for this case, the vortices shed by the body deliver considerable momentum to it.

Even for uniform flows, it is well known that these forces are of major concern to offshore civil structures (Sarpkaya, 1979; Lighthill, 1986a, 1986b). Moreover, Jordan and Fromm (1972) showed that a cylinder in a weak shear flow experiences an instantaneous lateral force due to vortex shedding which is approximately 16 times larger than the average lateral force produced by shear. In view of all this evidence, it is surprising how little attention has been given by the multiphase flow community to vortex shedding and wake effects on lateral forces.

It is interesting to compare the magnitude of vortex shedding induced forces in an uniform flow with those predicted by inviscid theory for a shear flow. Inviscid theory predicts $C_L = 2$ in Eq. (1) for a circular cylinder (Batchelor, 1967; Auton et al., 1988) submerged in an uniform shear flow. On the other hand, the lift coefficient due to vortex shedding in an uniform flow, $C_{L(aero)}$, is usually defined by analogy to the drag coefficient and it reaches maximum instantaneous values of $C_{L(aero)} = 1$ (Sarpkaya, 1979). Therefore, in order for the maximum lateral force due to vortex shedding on a cylinder in an uniform flow to be equal to the lift force on the cylinder in a shear flow, the magnitude of the average vorticity, ω, has to be such that $\omega D/v_r = 1/\pi$, where D is the cylinder diameter. Typical sizes and relative velocities of the particles in many multiphase flow applications are $D = 1$ mm and $v_r = 0.3$ m/s, respectively. Therefore, the vorticity would have to be of the order of $\omega = 100\ s^{-1}$ for vortex shedding forces and inviscid lift to be comparable. Significantly, this magnitude of the shear is found close to the pipe wall in a fully developed flow (Alajbegović, 1994; Alajbegović et al., 1994). It could be objected that in this comparison two- and three-dimensional geometries were mixed indiscriminately. However, it is doubtful that the influence of the geometry would affect the order of magnitudes of the estimated vorticity, ω. A similar comparison that does not mixes different geometries is carried out below.

It is well known that the helicoidal and zigzag trajectories observed in rising bubbles are due to vortex shedding (Saffman, 1956; Kelly and Wu, 1997; Fan and Tsuchiya, 1990). Because of the absence of direct measurements of forces it is more convenient to compare the typical velocities of lateral displacement for both, zigzag motion and inviscid lift. Ford and Loth (1997) measured the amplitude and periods of the zigzag motion of bubbles having two and three millimeters nominal diameter in a quiescent and a turbulent shear flow. The average lateral velocity of the zigzag motion ranged from 9×10^{-3} to 20×10^{-3} m/s. The lateral relative velocity of displacement, u_r, for inviscid lift in an uniform shear flow can be derived from an equilibrium balance of the drag and lift forces as, $u_r = (4C_L/3C_D)D\omega$. The mean shear used by Ford and Loth (1997) was $\omega \simeq 3\ s^{-1}$, which for a lift coefficient of $C_L = 0.1$ and a drag coefficient of $C_D = 0.44$, produce a lateral relative velocity of $u_r = 2 \times 10^{-3}$ m/s, which is five to ten times smaller than the observed average velocity of the zigzag motion.

From the two comparisons just made, it is clear that average lateral forces due to vortex shedding in a shear flow should be expected to be at least of the same order of magnitude as those of inviscid lift.

It is important to stress that the helicoidal and zigzag regimes are observable even in non-quiescent turbulent flows. This is confirmed not only by Ford and Loth (1997) but also by exploratory experiments carried out in this study. After examining the experimental evidence, Fan and Tsuchiya (1990) suggested that the stability of the zigzag regime is due to the fact that

it minimizes the wake size and consequently the energy dissipation. Therefore, the zigzag regime should be understood to be a resonance phenomenon in which the bubble and the shed vortices movements lock-in (Kelly and Wu, 1997; Fan and Tsuchiya, 1990). In fact, Fan and Tsuchiya (1990) were able to explain relevant features of the zigzag regime by considering the bubble and its primary, or effective, wake as a single rigid body, which represents a clear indication that even for deformed bubbles, bubble-wake interactions cannot be neglected.

The stability of the zigzag regime, the evidence that forces due to vortex shedding can be larger than forces due to inviscid lift, and the apparent reversal of the sign of the lateral forces in sudden expansions and developing flows, indicate that the current modeling of lateral forces in the two-fluid model is incomplete. Lateral forces due to vortex shedding, and other wake effects, have not been introduced into the closure laws used by the two-fluid model. Unfortunately, the complex wake geometry and the difficulties associated with an analytical treatment make lateral forces induced by vortex shedding difficult to quantify. Even though the wake of a fixed sphere in both a uniform flow and a shear flow has been characterized (Sakamoto and Haniu, 1990, 1995), it is not clear how the wake structure would be modified for a freely moving sphere. The problem of the interactions of the wake and its body movement is so complex that most researchers have considered it only for the particular case of forced oscillations in two dimensions (Stansby, 1976; Sarpkaya, 1979). Secondly, vortex shedding induced lateral forces were expected to be averaged out of the equations of motion if sufficiently long periods of time, or sufficiently large number of events, were considered.

It is clear that to gain the physical insight necessary to extend the two-fluid model to other geometries of interest it is necessary to understand and quantify the effects of vortex shedding on lateral forces for bluff three-dimensional bodies. This quantification is a very challenging task for Computational Fluid Dynamics (CFD) because of the high Reynolds numbers involved and the inherent unsteadiness and three-dimensionality of the problem, all factors that increase computational cost. Dandy and Dwyer (1990) calculated lift and drag forces on spheres in a uniform shear flow for Reynolds numbers lower than 100. The low Reynolds number was necessary to avoid the boundary layer separation that makes the problem unsteady. As mentioned above, previous computer simulations of deformable bubbles have been restricted to low Reynolds numbers for the same reason. Alajbegović et al. (1998) and Jordan and Fromm (1972) were able to simulate the unsteady behavior of the wake produced by a rigid bluff body because of the two-dimensionality of the problem.

Interestingly, most experimental work on the measurement of lateral forces on bubbles and rigid spheres has concentrated on flows not needing a statistical approach. This has been done mainly through the elimination of boundary layer separation by considering only low Reynolds numbers (Kariyasaki, 1987; Cherukat et al., 1994), or by designing levitation experiments for which a stable equilibrium point exists (Naciri, 1992; Eichhorn and Small, 1964; Yamamoto et al., 1993, 1995). In the later cases, lateral forces due to the shear are inferred from the equilibrium position and the other forces of known magnitude (e.g., drag, buoyancy and virtual mass). In the case of Naciri (1992) and Eichhorn and Small (1964), the need for a stable equilibrium point makes it possible to consider only moderate vortex shedding instabilities and consequently limits the range of the Reynolds number considered. Yamamoto et al. (1993, 1995) used pendants in order to create an equilibrium position through the restitutive force introduced by the pendant rod. Considering tethered particles rather than free moving particles

allows one to eliminate transient injection forces, which usually limit repeatability. Indeed, the lack of repeatability over the size ranges for which the helicoidal and zigzag trajectories are observed has been attributed to varying injection conditions in the experimental setup of different researchers (Saffman, 1956; Fan and Tsuchiya, 1990). Due to turbulence fluctuations and wake instabilities the determination of the average forces from the trajectories of free moving solid particles in a shear flow rapidly becomes prohibitively expensive. That is, except for limiting cases of a very well controlled turbulence structure and fluid density much smaller than the particle density (Yamamoto et al., 1993), the number of trajectories to be ensemble averaged in order to achieve repeatability easily surpass the acquisition, storage and processing capabilities of most commercially available video equipment. This fact is clearly observable in the results of Taeibi-Rahni and Loth (1996).

Particle image velocimetry (PIV) is a promising technique for the measurement of lateral forces, since it allows the determination of the instantaneous velocity field. Therefore, the validity of Eq. (1) (Ford and Loth, 1997) and the instantaneous forces due to vortex shedding (Lin and Rockwell, 1996) can, in principle, be quantified. Sridhar and Katz (1995) successfully used PIV to measure drag and lift coefficients on bubbles entrained in a vortex for small Reynolds numbers, $Re<80$.

In the present study, the analysis made by Lighthill (1986b) to quantify the form of the drag coefficient at high Reynolds numbers was extended to the lift coefficient. It will be shown that the functional dependance of the average vortex shedding-induced lateral forces is of the same form as that given in Eq. (1). Hence, the reduction from the predicted inviscid lift coefficient, $C_L = 1/2$, to the lower values of C_L which fits the existing data, may be explained by attributing it to wake effects and the related vortex shedding. Moreover, this argument suggests that the sign reversal found by Yamamoto et al. (1993, 1995) may be due to wake-induced lateral forces being dominant over inviscid lift. This hypothesis was confirmed by an experiment designed to measure the lateral forces on rigid spheres submerged in an uniform shear flow.

The experiment presented herein was motivated by the desire to quantify the effect of vortex shedding instabilities on the lateral forces at reasonably high values of the Reynolds numbers based on relative velocity, $Re = v_r D/\nu$, and average vorticity, $Re_\nabla = \omega D^2/\nu$, where ν is the kinematic viscosity. A tethered pendant was used to keep the particle around an equilibrium point, but unlike the experiments of Yamamoto et al. (1993, 1995), a statistical approach was used to obtain the average effect of the vortex shedding instabilities. The amount of information which needed to be acquired was kept to a minimum by the use of two parallel laser beams and the acquisition of the time sequence of beams interruptions by the pendant's thread. Therefore, with modest resources it was possible to acquire enough statistics to ensure repeatability.

In Section 2 the average lateral lift force induced by the wake was found to follow a form similar to that of Eq. (1). In addition, the dynamics of a pendant submerged in a uniform shear flow was examined in order to quantify differences in the dynamics of a free moving particle and a tethered pendant. Sections 3 and 4 present the method used to generate a turbulent uniform shear flow and the measured average velocity fields, respectively. Section 5 gives an exposition of the experimental method and results of the pendant experiments carried out for rigid spheres of different size and density, for several different water flow rates. In

accordance with the analysis in Section 2, the lateral forces were found to correlate with the product of the Reynolds number, $Re\,Re_{\nabla}$. Finally, a comparison with the work of other researchers was done and it is presented in this section.

2. Identification of phenomena of interest

2.1. Wake influence on the lateral forces for spheres in an uniform shear flow

Several expressions have been proposed over the years to quantify the lateral force on a particle in a shear flow. For viscous flow, Saffman (1965, 1968) and Bretherton (1962) derived the force on a sphere and a cylinder, respectively. However, their results will not be considered any further because their work was only concerned with inertia dominated flows. As noted previously, Drew and Lahey (1987, 1990), Auton (1987), and Auton et al. (1988) independently derived Eq. (1) for the inviscid lift force on a sphere. For pipe flow this can be written as,

$$F_{\mathrm{L(inviscid)}} = \rho C_{\mathrm{L}} V v_{\mathrm{r}} \frac{d\omega}{dr} = \rho C_{\mathrm{L}} V v_{\mathrm{r}} \omega \tag{2}$$

where v_{r} is the relative velocity between the sphere and fluid, ω is the axial velocity of the continuous phase, and for a sphere submerged in an inviscid fluid, $C_{\mathrm{L}} = 0.5$. This expression has been widely used in computer code implementations of the two-fluid model (Alajbegović, 1994; Lahey et al., 1993; Wang, 1986; Wang et al., 1986; Bel Fdhila, 1991), where, because of viscous effects, C_{L} was used as a fitting coefficient. Although the optimum value of this coefficient can change from one flow configuration to another, $C_{\mathrm{L}} = 0.1$ has been successfully used for predictions of fully developed bubbly two-phase flow in a vertical pipe.

The reduction of the coefficient value from 0.5 to 0.1 has been attributed to turbulence (Wang et al., 1986) and to the presence of a wake (Alajbegović, 1994), both of which were neglected in the inviscid analysis. The size of the wake, which is generally of the same order as that of the immersed object itself, is an obvious indicator that its effect on body forces cannot be neglected. Moreover, it is well known that, even in uniform flow, lateral forces induced by vortex shedding cannot be overlooked in the analysis leading to the design of immersed bodies (Lighthill, 1986b).

Unfortunately, an accurate determination of the magnitude of the lift force induced by vortex shedding is very difficult, the main problems being the complexity of the wake structure and its elusiveness to an analytical treatment. However, considerations of the kinetic energy in the wake can prove useful to identify the functional dependance of the wake-induced lateral forces on bluff bodies. What follows is an extension to the lift coefficient of the usual argument accepted for justifying the functional dependance of the drag coefficient (Lighthill, 1986b). Due to the importance of the wake's geometry a description of it for different cases is presented first.

When a vortex is shed, the space it occupied behind the body is replenished by liquid moving more slowly than the rotational velocity of the vortex. A significant velocity reduction occurs due to the sharp turn that the incoming fluid has to make to occupy the volume immediately after the body. The Bernoulli equation predicts that this decrease in the velocity of

the fluid will generate an increase in pressure. Therefore, when a vortex is shed, a transient lateral force on the body will arise. After averaging over an appropriately long period of time, this effect will generate a non-zero lateral force if the wake is not symmetric with respect to a plane perpendicular to the direction of the lateral force, parallel to the main direction of the flow and passing through the center of the body (i.e., the centerline plane). This is necessarily the case for a shear flow. The numerical simulations of Jordan and Fromm (1972) and Alajbegović et al. (1998) show very clearly how this mechanism may produce a non-zero average lateral force.

The lateral force will depend significantly on the wake structure, but two cases need to be considered. In the first case, which can be found in cylinders of circular and non-circular cross-section (Alajbegović et al., 1998; Jordan and Fromm, 1972), the high and low velocity sides periodically shed vortices which differ in size and characteristic velocity. As a consequence the lateral force changes sign over time. A non-zero average lateral force arises because the lateral force produced by shedding on the high velocity side is different in magnitude from that originated by shedding on the low velocity side. The net force is toward the low velocity side. In the second case, which has been found in a fixed sphere in uniform shear flow (Sakamoto and Haniu, 1995), vortices form and detach at the high velocity side only. Vortices at the high velocity side grow faster and bigger than those at the low velocity side and eventually they engulf the latter before they form a separate vortex and detach. Therefore, vortices covering the whole cross stream span of the wake are observed. They are strongly non-symmetric with respect to the centerline plane. Thus, even in the absence of shedding from the low velocity side there is a lateral force, although in this case periodic changes of sign are not expected. The shape of the hairpin vortices visualized by Sakamoto and Haniu (1995) suggests that the force is toward the low velocity side for a fixed sphere, as well as in the case of the cylinder. Taking into account the direction of the relative velocity and the vorticity, we find that this direction is opposite to that predicted by inviscid lift for a sphere.

Thus, it is to be expected that the total lateral force on a sphere results from a balance of inviscid effects as accounted for in traditional inviscid theory (Drew and Lahey, 1987, 1990; Auton, 1987; Auton et al., 1988) and wake effects. Significantly, no vortex shedding is expected for Reynolds numbers below 300 (Sakamoto and Haniu, 1995) and consequently inviscid effects should be dominant. As the Reynolds number increases wake effects become more important until they reverse the sign of the lateral force.

It is not clear which of the two cases noted above the wake of a free moving sphere in a shear flow resembles more, but it seems likely that it is in some intermediate stage between the two. That is, the movement of the sphere will increase the likelihood that a separation bubble generated on the low velocity side is not absorbed into the vortex loop formed at the high velocity side before it can grow into a separate vortex loop.

An estimate of the kinetic energy in the wake follows. The rate at which the mass of wake fluid grows is $\rho A(v_r + \omega D/2)/2$ on the high velocity side, and $\rho A(v_r - \omega D/2)/2$ on the low velocity side (see Fig. 1); where A is the body frontal area, ρ is the density of the liquid, D is the diameter of the immersed body (this argument is applicable to spheres and cylinders) and, in this context, and ω is the velocity gradient in a direction perpendicular to the main flow. Velocities in the vortex motion are proportional to the free stream velocity, giving a rate of increase of kinetic energy in the wake of:

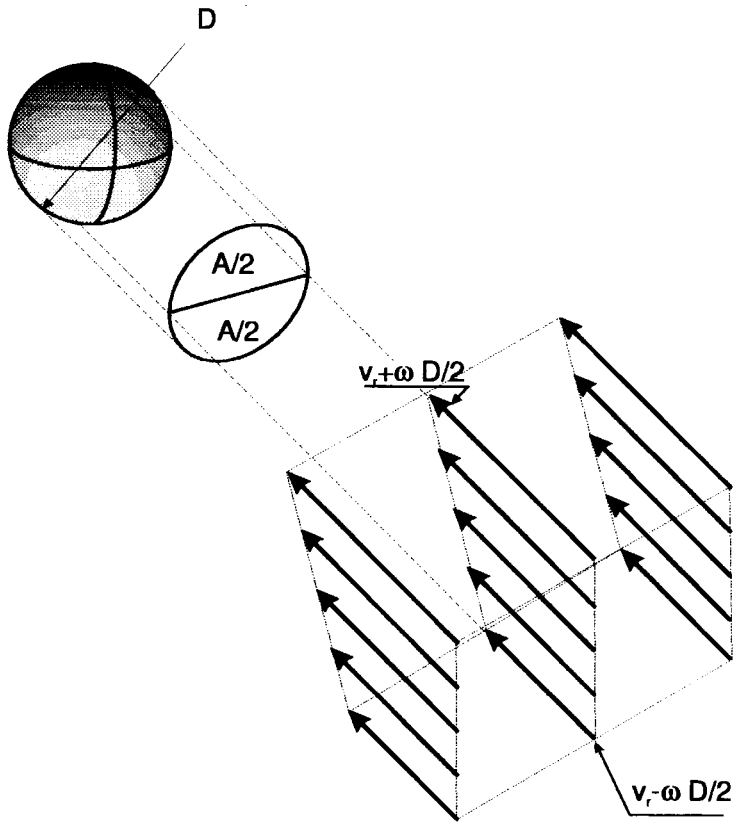

Fig. 1. Schematic of a sphere submerged in a uniform shear flow.

$$C_{1+}\rho A(v_r + \omega D/2)^3 \quad \text{and} \quad C_{1-}\rho A(v_r - \omega D/2)^3$$

for the high and low velocity sides, respectively, where $C_{1\pm}$ are the constants of proportionality linking the velocities in the mainstream, $v_r \pm \omega D/2$, and in the wake. Of course, this argument requires that averaging over time is carried out. Otherwise, relating velocities in the vortex region with that of the free stream through constants of proportionality does not make sense. Moreover, these constants could differ on each side due to asymmetries in the wake-induced by the shear.

Let us assume that the velocities of displacement in the lateral direction produced by the vortex shedding instabilities are also proportional to $(v_r \pm \omega D/2)$, hence, the lateral forces are proportional to

$$C_{Lw+}\rho A(v_r + \omega D/2)^2/2 \quad \text{and} \quad C_{Lw-}\rho A(v_r - \omega D/2)^2/2$$

where $C_{Lw\pm}$ is the product of $C_{1\pm}$ and another constant of proportionality, relating the mainstream velocities with the lateral velocities.

Clearly, there is no need for C_{Lw+} and C_{Lw-} to be equal. In particular, evidence that they are not equal for the fixed sphere case was discussed above. However, it is to be expected that

these differences will not be as strong for a moving sphere as for a fixed one. Because of this let us assume that the coefficients are the same at both sides, hence: $C_{Lw} = C_{Lw+} = C_{Lw-}$.

For the first case, alternate vortex shedding on the high and low velocity sides, the vortices shed on each side should produce forces of opposite directions. For the second case (the fixed sphere) as a hairpin vortex is shed, a net force arise from the simultaneous competitive effects on each side. Therefore, in both cases the average lateral force induced by vortex shedding will be (where $\langle\ \rangle$ denotes time averaging):

$$\left\langle F_{L(wake)} \right\rangle = \frac{C_{Lw}}{2}\rho A\left[(v_r + \omega D/2)^2 - (v_r + \omega D/2)^2\right]$$

$$= C_{Lw}\rho A D v_r \omega \tag{3}$$

which is the same functional dependance as inviscid lift, Eq. (2), because AD is directly proportional to the volume of the body. An immediate corollary can be derived from this finding: to accommodate wake effects it is possible to have a new coefficient in the inviscid lift relationship and to use it to fit the experimental data. This is the approach which has been taken implicitly in two-fluid modeling. The fact that most published data on bubbly (Wang et al., 1986; Lahey et al., 1993) and solid/liquid (Alajbegović et al., 1994) two-phase flow imply that the lift coefficient ranges between 0.01 and 0.1, a range of values considerably smaller than the 0.5 predicted by inviscid theory, implies that wake effects induce forces in the opposite direction and with the same functional dependance. Moreover, it suggest why negative values of C_L are necessary to fit experimental data for bubbly two-phase flow in a sudden expansion (Bel Fdhila, 1991) and for some developing flows in a vertical pipe (Grossetete, 1995).

The absence of the sphere's density, ρ_d, in Eq. (3) is significant. In most multiphase flow applications the dispersed body will move under the influence of the lateral forces induced by the wake. This movement will displace the body which in turn will modify the wake structure. This modification can cause such phenomena as lock-in (i.e., the synchronized movement of bubbles and their wakes (Saffman, 1956)). As soon as the sphere is allowed to move its density plays a role. However, the problem is so complex that even for two dimensions most researchers choose to simplify it by considering only the case of forced oscillations (Stansby, 1976). Alajbegović et al. (1994) explained his finding that the lift coefficient for light particles is smaller than that of heavy ones because the shear flow rotates the former more easily than the latter. This rotation induces a Magnus force and a very non-axisymmetric wake. Negative lift coefficients have been observed by several researchers for rotating spheres (Maccoll, 1928; Davies, 1949; Taneda, 1957). For this case the wake-induced lateral force could have a more complex form than in Eq. (3) because of the constants of proportionality not being equal; however, the reasoning leading to Eq. (3) is still valid. Moreover, in this particular case the constants C_{Lw+} and C_{Lw-} should be strongly influenced by the shear magnitude and the sphere's density.

Another factor that can dramatically influence the wake structure and consequently the lateral forces that it originates is the incoming fluid turbulence. Kim and Durbin (1988) found that acoustic excitation can dramatically affect the vortex shedding frequency and the drag coefficient. Torobin and Gauvin (1960) also found that turbulence of the surrounding liquid is

a major factor in determining the value of the critical Reynolds number at which boundary layer separation occurs. The ratio of the characteristic size, l, of the energy carrying eddies of the liquid flow and the sphere's diameter, D, determines the relative importance of the lateral forces induced by the mean shear of the flow on one hand, and the turbulence dispersion on the other. It is to be expected that as this ratio increases the value of the coefficient C_{Lw} diminishes.

It is convenient to explore how the inviscid lift and wake-induced lateral forces add up. Choosing a coordinate system with the origin at the center of the sphere, the case of uniform shear flow is described without loss of generality by assuming $v_r = (0,0,w_r + \omega x)$. Therefore, Eq. (2) becomes,

$$F_{L(\text{inviscid})} = \rho C_L V \omega w_r \tag{4}$$

where $F_{L(\text{inviscid})}$ is in the x direction. To write Eq. (3) for the selected frame of reference w_r has to be replaced by v_r. Hence, from the sum of Eqs. (4) and (3) the total time-averaged lateral force, $\langle F_L \rangle$, on a sphere is,

$$\langle F_L \rangle = \left\langle F_{L(\text{inviscid})} \right\rangle + \left\langle F_{L(\text{wake})} \right\rangle$$

$$= \rho V(-C_L + C_{Lw})\omega w_r = C_{LT}\rho V \omega w_r \tag{5}$$

where the constant geometric factor AD/V has been absorbed in C_{Lw} and the elementary properties of the time-averaging operator were applied. The non-dimensional form of Eq. (5) is,

$$\frac{\langle F_L \rangle}{\pi \rho \nu^2/6} = C_{LT} Re\, Re_\nabla \tag{6}$$

where,

$$Re = w_r D/\nu \quad \text{and} \quad Re_\nabla = \omega D^2/\nu \tag{7}$$

are the relative velocity and velocity gradient Reynolds numbers, respectively, and ν is the kinematic viscosity of the continuous phase. In Eq. (6), C_{LT} is the total lift coefficient given by the sum of inviscid and wake effects, which, for a sphere becomes,

$$C_{LT} = C_{Lw} - \frac{1}{2} \tag{8}$$

It is assumed that the directions of the inviscid and wake effects are opposed and to facilitate the exposition of experimental results the wake induced force direction is adopted as being positive. The use of the constant value 1/2 for the inviscid lift is based on the analysis of Drew and Lahey (1987, 1990), Auton (1987) and Auton et al. (1988). As in the case of the drag argument presented by Lighthill (1986b), the constants of proportionality used in this exposition have to depend on the flow structure and consequently on the Reynolds numbers and length scales of the flow. Thus, based on all the considerations discussed above it is to be expected that,

$$C_{\mathrm{Lw}} = C_{\mathrm{Lw}}\left(Re, Re_{\nabla}, \frac{\rho}{\rho_{\mathrm{s}}}, \frac{l}{D}\right)$$

Therefore, C_{LT} in Eq. (8) should be a function of Re and Re_{∇}. Similarly, the drag coefficient is a function of the Reynolds number, Re (Lighthill, 1986b).

2.2. The pendant equation

The equation describing the motion of a rigid discrete pendant sumberged in a fluid for an inertia dominated flow with instantaneous drag, $\mathbf{D}$, and lift forces, $\mathbf{L}_{\mathrm{I}}$, (Auton et al., 1988; Loth et al., 1997; Naciri, 1992) is:

$$\left(\rho_{\mathrm{d}} + C_{\mathrm{VM}}\rho\right) V_{\mathrm{d}} \frac{\mathrm{d}\mathbf{v}_{\mathrm{d}}}{\mathrm{d}t} = -V_{\mathrm{d}}(\rho_{\mathrm{d}} - \rho)g + \mathbf{D} + \mathbf{L}_{\mathrm{I}} + V_{\mathrm{d}}\rho(1 + C_{\mathrm{VM}})\frac{D\mathbf{v}}{Dt} + \mathbf{L}_{\mathrm{W}} \tag{9}$$

where $\mathbf{v}$ and $\mathbf{v}_{\mathrm{d}}$ are the liquid and pendant velocity, respectively, ρ_{d} and ρ are the sphere and fluid density, respectively, and g is the acceleration of gravity. The parameters V_{d} and C_{VM} are the volume and virtual volume coefficient of the body, which for the particular case of a sphere become $\pi D^3/6$ and $1/2$, respectively. The fourth term on the right-hand side involves the fluid's material derivative, $D/Dt = \partial/\partial t + \mathbf{v}\cdot\nabla$, and arises because, as the fluid field changes in space and time, it induces forces on the body. The last term, $\mathbf{L}_{\mathrm{W}}$, represents the lateral forces due to the interaction of the body and its wake. This force is usually not modeled and is taken into account by changing the value of a coefficient in the inviscid lift force, $\mathbf{L}_{\mathrm{I}}$. In most applications for turbulent flows, Eq. (9) can only be evaluated in terms of average quantitites because neither enough detailed knowledge of the velocity field, nor computing power, is available. Because of the accurate determination of the average velocity field, this work represent a unique opportunity for assessing the hypothesis necessary to write Eq. (9) in terms of the average liquid velocities. Hence, a brief exposition of these hypothesis for the particular velocity field relevant for this investigation follows.

In term of average quantities the flow is steady,

$$\frac{\partial}{\partial t} \equiv 0, \tag{10}$$

and has the following spatial dependance in the neighborhood of the particle,

$$\begin{cases} w = w_0 + \omega x & \text{(axial velocity)} \\ u << w_0 & \text{(lateral velocity)} \\ v = 0 & \text{(spanwise velocity)} \end{cases} \tag{11}$$

Although the mainstream velocity at the tethered pendant's rest position, w_0, does depend on the z coordinate, for the case of a pendant the z dependance can be safely neglected. Because the liquid velocity in the x direction, u, is much smaller than w_0, and since the x range of the pendant is very small, spatial derivatives of u can also be neglected. The accuracy of Eqs. (10) and (11) depends strongly on the time and length scales of the turbulence being small compared with their pendant counterparts. The small size of the non- uniform grid wires used to establish the shear flow, compared with the spheres used, suggests that turbulence length

scales are small enough for Eqs. (10) and (11) to hold. Similarly, the flatness of the root mean square velocity profiles (see Section 4) suggest that is safe to assume there are no turbulent-phoretic forces. Eqs. (10) and (11) can be replaced in $D\mathbf{v}/Dt$ to show that in the direction perpendicular to the tether attached to the pendant, $D/Dt \equiv 0$. Thus, in this direction,

$$\left(\rho_d + C_{VM}\rho\right)V_s L\frac{d^2\theta}{dt^2} = -V_s(\rho_d - \rho)g\sin\theta + (\mathbf{D} + \boldsymbol{L}_I + \boldsymbol{L}_W)_\theta \tag{12}$$

where θ is the angle formed by the thread with the vertical and it is positive moving toward the low velocity side, that is, in the x positive direction. Hence, L is the distance between the pendant hanging point and its center of mass and the subscript θ indicates the direction perpendicular to the tether. In this direction, the drag force can be written as,

$$\mathbf{D}_\theta = -\frac{C_D}{8}\rho\pi D^2\sqrt{\left(u - L\frac{d\theta}{dt}\cos\theta\right)^2 + \left(w + L\frac{d\theta}{dt}\sin\theta\right)^2} \times \left(L\frac{d\theta}{dt} - u\cos\theta + w\sin\theta\right) \tag{13}$$

To obtain this expression the absolute value of the relative velocity of the sphere with respect to the fluid is used to calculate drag, which is then projected in the direction perpendicular to the tether. It will be seen in the Section 4 that $w \gg Ld\theta/dt, u$. Thus, Eq. (13) can be simplified to:

$$\mathbf{D}_\theta = \frac{C_D}{8}\rho\pi D^2|w|\left(L\frac{d\theta}{dt} - u\cos\theta + w\sin\theta\right) \tag{14}$$

The combined effects of inviscid lift and the wake-induced lateral forces are written as,

$$(\mathbf{L}_I + \mathbf{L}_W)_\theta = C_{LT}(t)\rho V_d w\omega\cos\theta \tag{15}$$

Note that to include wake induced instabilities the parameter $C_{LT}(t)$ should be a function of time.

Replacing Eqs. (14) and (15) in (12) and rearranging yields,

$$\frac{d^2\theta}{dt^2} + \frac{1}{\tau_D}\frac{d\theta}{dt} = -\frac{1}{\tau_v^2}\sin\theta + \frac{1}{\tau_h^2(t)}\cos\theta \tag{16}$$

where

$$\frac{1}{\tau_D} = \frac{3C_D\rho|w|}{4\left(\rho_d + C_{VM}\rho\right)D} \tag{17}$$

$$\frac{1}{\tau_v^2} = \frac{(\rho_d - \rho)g}{\left(\rho_s + C_{VM}\rho\right)L} + \frac{3C_D\rho w^2}{4D\left(\rho_d + C_{VM}\rho\right)L} \tag{18}$$

and

$$\frac{1}{\tau_h^2(t)} = \frac{3C_D\rho|w|u}{4D(\rho_d + C_{VM}\rho)L} - \frac{C_{LT}(t)\rho w\omega}{(\rho_d + C_{VM}\rho)L} \tag{19}$$

Eq. (16) is the well-known equation of a damped pendant with an extra forcing term, $\cos\theta/\tau_h^2(t)$, due to the lateral or horizontal forces (the subscripts 'h' and 'v' stand for horizontal and vertical, respectively). Solving Eq. (16) requires knowledge of the unknown time dependance of $\tau_h^2(t)$. However, for the purpose of this discussion the time-average form of Eq. (16) at a fixed θ is more relevant. After rearranging we have:

$$\langle\tan\theta\rangle = \left\langle\frac{1}{\tau_h^2(t)}\right\rangle\tau_v^2 - \left\langle\frac{d^2\theta}{dt^2} + \frac{1}{\tau_D}\frac{d\theta}{dt}\right\rangle\frac{\tau_v^2}{\cos\theta} \tag{20}$$

We note that $\tan\theta$ has not been completely specified, since in Eq. (20) $\cos\theta$ appears in the right-hand side. However, the smallness of the values of θ involved (see Section 6) allows one to assume that $\cos\theta \approx 1$. It must be stressed that because of vortex shedding instabilities, the drag coefficient should be considered a function of time also. However, Jordan and Fromm (1972) predict for a cylinder in a shear flow a variation with time smaller than 10% and larger than 100% for the drag and lift coefficients, respectively. Based on this evidence, the drag variation with time was expected to be much less than that of lift. Thus, the drag coefficient was considered to be constant. Thus, both τ_h^2 and τ_D are considered constants with respect to time. Without the second term on the right-hand side, Eq. (20) describes a static balance of forces including buoyancy, drag and the time-averaged lateral forces. The second term describes the time-averaged force produced by accelerations and damping. For symmetric oscillations around a equilibrium angle, θ_{eq}, which is not necessarily zero:

$$\left\langle\frac{d^2\theta}{dt^2} + \frac{1}{\tau_D}\frac{d\theta}{dt}\right\rangle_{\theta=\theta_{eq}} = 0 \tag{21}$$

If the oscillations are symmetric for each positive angular acceleration, there will be a negative one with the same value. Thus, if time integration occurs during a long enough interval, the average acceleration will be zero. A similar argument applies to angular velocity. However, not all oscillation modes are symmetric as will be seen in a later example in this section. Because the experimental method is based on the indirect determination of lateral forces though the measurement of an angle, θ_{eq}, and a static balance of forces, it is important to study the consequences of Eq. (21) not being valid. The static force balance at θ_{eq} renders,

$$\tan\theta_{eq} = \left\langle\frac{1}{\tau_h^2(t)}\right\rangle\tau_v^2 - \left\langle\frac{d^2\theta}{dt^2} + \frac{1}{\tau_D}\frac{d\theta}{dt}\right\rangle_{\theta=\theta_{eq}}\frac{\tau_v^2}{\cos\theta_{eq}} = \left\langle\frac{1}{\tau_h^2(t)}\right\rangle_m\tau_v^2 \tag{22}$$

where $\langle 1/\tau_h^2(t)\rangle_m$ is the measured time-averaged contribution of the lateral forces and τ_v^2 is known since all magnitudes in Eq. (18) are known. Thus, the measured and the actual time-averaged lateral forces differ by a term proportional to $\langle\frac{d^2\theta}{dt^2} + \frac{1}{\tau_D}\frac{d\theta}{dt}\rangle_{\theta=\theta_{eq}}$. After multiplication by the length, L, this average can be interpreted as the contribution of lateral accelerations and viscous forces. Since a similar term would exist for a free particle in a shear flow, judging the

$\langle \frac{d^2\theta}{dt^2} + \frac{1}{\tau_D}\frac{d\theta}{dt}\rangle_{\theta=\theta_{eq}}$ term to be an experimental error is premature. For fully developed bubbly flow in a pipe it is usually assumed that there is no radial velocity, the assumption being justified because the flow is fully developed. Hence, in applying the experimental results of this work to this particular case the issue to address is how much the $\langle \frac{d^2\theta}{dt^2} + \frac{1}{\tau_D}\frac{d\theta}{dt}\rangle_{\theta=\theta_{eq}}$ term differs from its free particle counterpart. This question could be rephrased as, how much the constraint imposed by the fixed distance between the hanging point and the sphere affects the wake dynamics. This question will be addressed later in light of the experimental evidence in Section 7. If the lateral velocity field is to be resolved, then the $\langle \frac{d^2\theta}{dt^2} + \frac{1}{\tau_D}\frac{d\theta}{dt}\rangle_{\theta=\theta_{eq}}$ term should be considered as an experimental error and the issue to address is how much error it introduces; that is, how large it is compared to $\langle 1/\tau_h^2(t)\rangle$. Again, this issue will be analyzed in Section 7.

To further explore the error introduced by $\langle \frac{d^2\theta}{dt^2} + \frac{1}{\tau_D}\frac{d\theta}{dt}\rangle_{\theta=\theta_{eq}}$ and to obtain some magnitudes relevant to the experimental analysis of data, the particular cases of a constant lift coefficient will be explored. Thus, it is assumed that,

$$C_{LT}(t) = C_{LT0} \tag{23}$$

Although Eq. (16) can readily be solved numerically, for the purpose of this exposition the analytical solution obtained after introduction of the small angle approximations, $\sin\theta \simeq \theta$ and $\cos\theta \simeq 1$, are sufficient. The approximations introduce errors in θ smaller than 5×10^{-5} and 2×10^{-3}, respectively, both of which are negligible compared with the experimental error, as it will be seen in Section 6.2. With these approximations Eq. (16) can be written as,

$$\frac{d^2\theta}{dt^2} + \frac{1}{\tau_D}\frac{d\theta}{dt} + \frac{1}{\tau_v^2}\theta = \frac{1}{\tau_h^2} \tag{24}$$

The above is the well-known equation of a damped harmonic oscillator with constant forcing $1/\tau_h^2$. Its solution for the initial conditions,

$$\theta(t=0) = \theta_0$$

$$\frac{d\theta}{dt}(t=0) = \dot{\theta}_0$$

is

$$\theta = \exp\left(-\frac{t}{\tau_D}\right)\left[\tau\left(\dot{\theta}_0 + \frac{\theta_0 - \theta_{eq}}{\tau_D}\right)\sin\frac{t}{\tau} + (\theta_0 - \theta_{eq})\cos\frac{t}{\tau}\right] + \theta_{eq} \tag{25}$$

where it was assumed that the discriminant,

$$-\frac{1}{\tau^2} = \frac{1}{\tau_D^2} - 4\frac{1}{\tau_v^2} \tag{26}$$

is smaller than zero. The constant particular solution, θ_p, to the non-homogeneous Eq. (24) is,

$$\theta_{eq} = \frac{\tau_v^2}{\tau_h^2} \tag{27}$$

The parameter $1/\tau$ is the natural frequency of the system. It is important to note that τ does not depend on the lateral forces. Thus, the main effect of lateral forces is to move the position around which oscillations occur from $\theta = 0$ to θ_{eq}.

Even though the oscillations are centered around θ_{eq}, the time-average of the first and second time derivatives of Eq. (25) evaluated at θ_{eq} will not be identically zero because of the exponential modulation of the amplitude. In other words, the sign of θ_0 gives preference to one side over the other.

Eq. (25) shows that the average value of θ depends on the lift coefficient through τ_h^2, and that $\langle \frac{d^2\theta}{dt^2} + \frac{1}{\tau_D}\frac{d\theta}{dt}\rangle_{\theta=\theta_{eq}}$ is not necessarily zero. However, since the lift coefficient in the presence of strong body-wake interactions is a complex, and not necessarily periodic, function of time, the motion of the pendant may be more complex than the described by Eq. (25). In general, it is possible to write,

$$\theta = \theta_{eq} + f(t) \tag{28}$$

where $f(t)$, is a function of time such that,

$$\int_0^T f(t)\,dt \to 0 \quad \text{as} \quad T \to \infty \tag{29}$$

The experimental error introduced by $\langle \frac{d^2\theta}{dt^2} + \frac{1}{\tau_D}\frac{d\theta}{dt}\rangle_{\theta=\theta_{eq}}$ will be negligibly small, if,

$$\frac{1}{T}\int_0^T \frac{d}{dt} f\,dt \to 0 \quad \text{as} \quad T \to \infty \tag{30}$$

$$\frac{1}{T}\int_0^T \frac{d^2}{dt^2} f\,dt \to 0 \quad \text{as} \quad T \to \infty \tag{31}$$

Evidence that this condition is satisfied for the non-periodic data will be presented in Section 6.1.

3. The production of a turbulent uniform shear flow using non-uniform grids

Yamamoto et al. (1993, 1995) measured the lift force on a solid sphere at high Reynolds numbers. They used a method designed by Owen and Zienkiewicz (1957) to produce a linear velocity gradient in a wind tunnel. The gradient was produced by a grid of parallel rods which were not equally spaced. Owen and Zienkiewicz derived the spacing of the rods in the grid needed to make the velocity gradient linear using a combination of small perturbations methods, inviscid theory before and after the grid, and experimental correlations at the grid itself. They tested their method with surprising success even for cases where the small perturbation hypothesis did not hold. This success reflects the fact that the experimental correlations used are not limited by the small perturbation hypothesis. This grid method has been used in single-phase turbulence studies by McCarthy (1964), Rose (1966, 1970), Borean et

al. (1995). Elder (1958) and McCarthy (1964) have also extended the method to non-linear velocity gradients.

All researchers used open air loop setups where the pumping power needed to reach very high Reynolds numbers (the Reynolds number based on the test section width ranges from 2×10^5 in Yamamoto et al. experiments to 8×10^5 in Owen et al.'s work) is not a concern. The value of the shear was adjusted by controlling the flowrate. Thus, for a given x position there exists a relation between the axial velocity, w, and the shear, $dw = dx$.

4. Continuous phase velocity field measurements

Schematics of the flow loop and test section can be seen in Figs. 2 and 3. Note that the water was directed downwards, and an elevated water storage tank was connected to the pump inlet to provide a constant pressure reference. A centrifugal pump was employed and the flow rate was adjusted using a set of calibrated throttle valves. The solidity distribution of the grid used to produce the shear can be seen in Fig. 4. A more detailed description of the experimental facility and the velocity measurement method can be found elsewhere (Moraga, 1998; Moraga et al., 1999). In order to cover a large range of Reynolds numbers, two different temperatures were used, $26 \pm 2°C$ and $55 \pm 2°C$. The kinematic viscosity of water decreases as

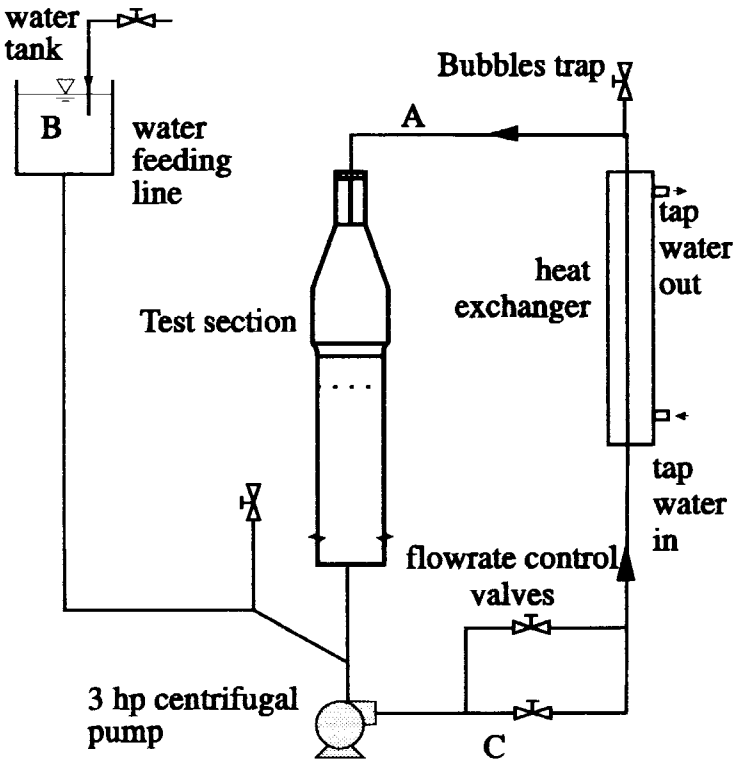

Fig. 2. Schematic of the loop.

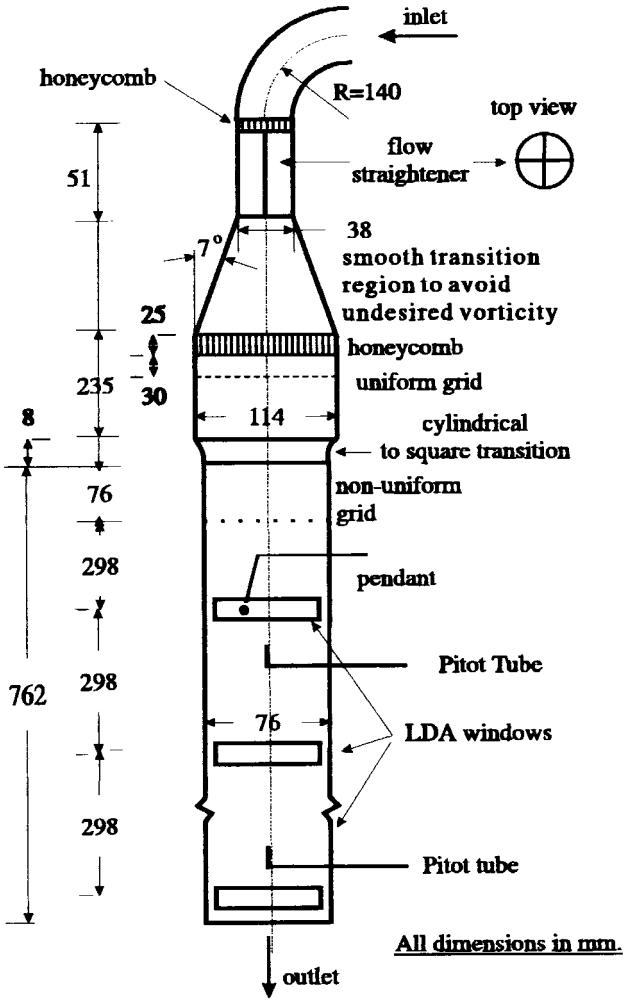

Fig. 3. Detail of the test section.

the temperature increases, thus, the Reynolds numbers increase with temperature. Fig. 5 shows a schematic of the reference system with respect to the grid. This figure will be useful for later reference.

4.1. Axial velocity, w

Let us now consider the measurements of the axial velocity, w.

4.1.1. Measurements at 55°C

Two sets of measurements for two different flow rates were acquired. Each flow rate is characterized by its centerline velocity at $z/h = 1$,

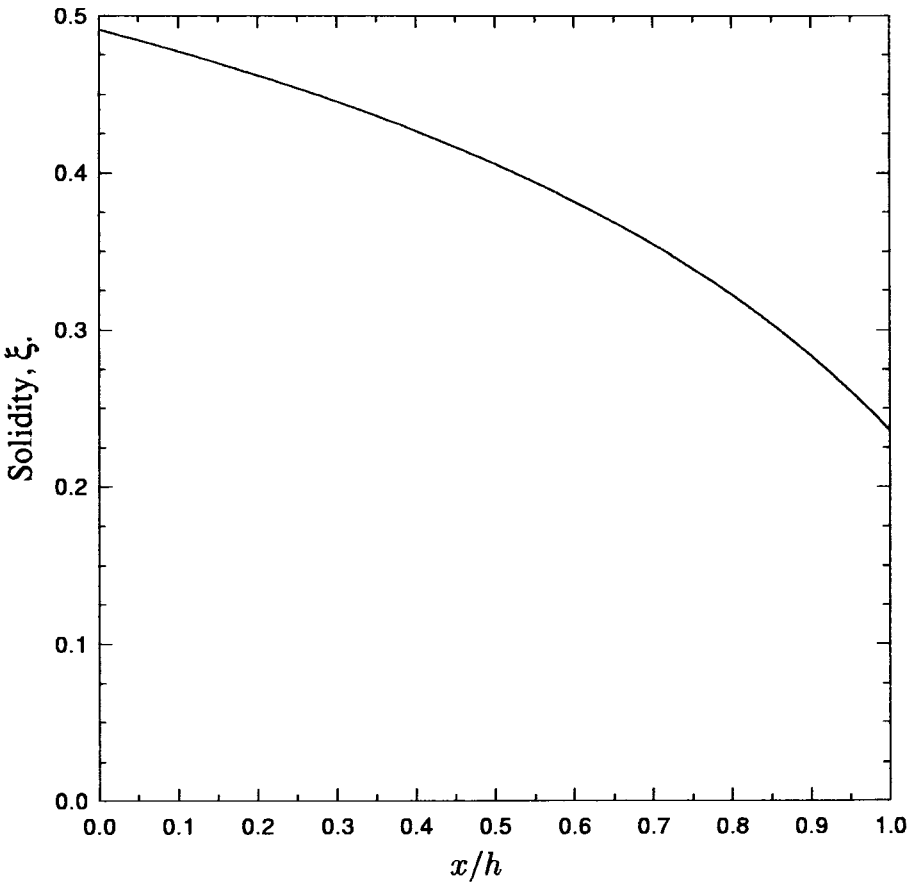

Fig. 4. Solidity distribution along the grid. Solidity, ξ, is the ratio of the wires diameter, d, and the distance between wire centers, s; that is, $\xi = d/s$.

$$w(x/h = 0.5, y/h = 0.5, z/h = 1) = 0.56;\ 0.67\ \text{m/s}$$

which from here on will be referred as the centerline velocity and $h = 76.2$ mm is the duct width. The 0.56 m/s set is the more extensive one since the 0.67 m/s one consisted of a repeatability check.

The results can be seen in Figs. 6–10, which show the mean and root mean square (rms) streamwise velocities, w, w_{rms}, respectively, as a function of position.

Table 1 shows the main results corresponding to $z/h = 1$ and $y/h = 0.5$. In the table $\mathrm{d}w/\mathrm{d}x$

Table 1
Main parameters for measurements at $z/h = 1$ and $y/h = 0.5$ at 55°C (w_{rms} is the average of all data points)

$w\|_{x/h=0.5}$ (m/s)	w_{rms} (m/s)	$\mathrm{d}w/\mathrm{d}x$ (1/s)	$\sigma\ 10^{-2}$ m/s	$\sigma/w\|_{x/h=0.5}$ (%)	r^2	Figures
0.56	0.051	7.81	3.0	5	0.959	Figs. 6 and 7
0.67	0.056	9.54	1.4	2	0.994	Figs. 8 and 9

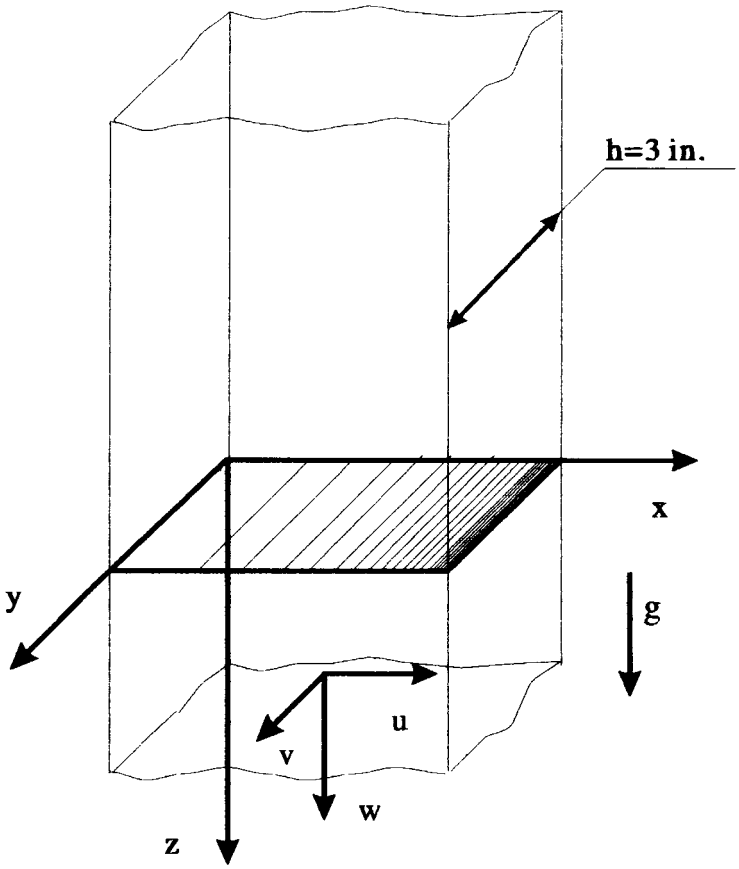

Fig. 5. Detail of the coordinate system.

is the fitted slope; w_{rms} is the average of all data points at $z/h = 1$ and $y/h = 0.5$ and corresponds to approximately 8% turbulent intensity. The standard deviation of the linear fit, σ, and the square of the correlation coefficient, r^2, are used as a measure of the linearity of the profile. Since σ is just 2 to 5% of the corresponding centerline velocity, $w|_{x/h=0.5}$, and it is smaller than w_{rms}, the results show a very acceptable degree of linearity.

Fig. 6 shows that the core of the flow is bidimensional at $z/h = 1$; that is, the velocity profile are practically the same at the central values of y/h ($=0.375$, 0.5, 0.625) and rise slightly closer to the walls ($y/h = 0.25$,0.75) without loosing linearity in the x direction. Fig. 7 shows the w_{rms} velocities corresponding to the 0.56 m/s centerline velocity at $z/h = 1$.

In order to determine the repeatability of the measurements, data were acquired on two different days for the same flow rate conditions (i.e., for a centerline velocity of 0.67 m/s). These results can be seen in Figs. 8 and 9. From the linear fits in Fig. 8 it can be seen that the lines for both dates are practically parallel and the main difference between the two sets is a small displacement of the curves, probably produced by a small change in the total flow rate. It is observed that this change is too small to be detected by the Pitot tube used to verify that the flow rate was constant along the measurements. The repeatability of the rms velocities is

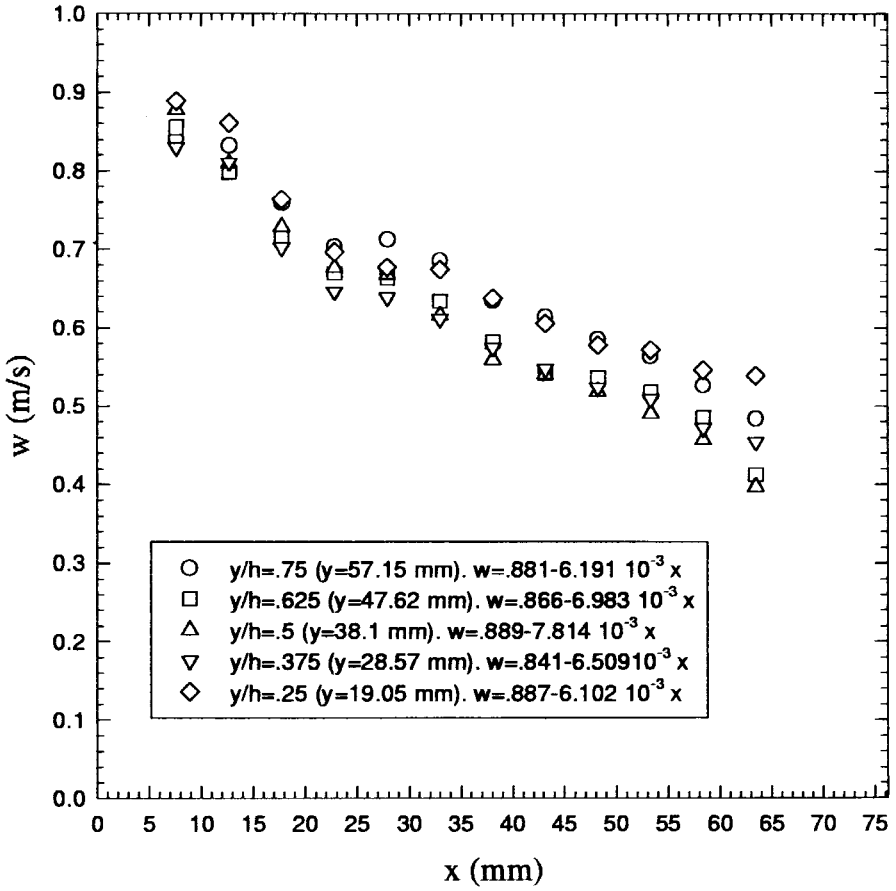

Fig. 6. Streamwise velocity profile at $z/h = 1$ for a centerline velocity of 0.56 m/s and at 55°C.

also excellent considering that they are a second-order momentum term and consequently they are more susceptible to statistical fluctuations.

As seen in Figs. 7 and 9, turbulence intensities are about 8% of the centerline velocity. This value is comparable to the 5% found by other researchers in air loops (Yamamoto et al., 1993). The increase in intensity can be attributed to the higher grid solidity required for the more compact grid used in this water loop. It can also be observed from Figs. 7 and 9 that the turbulence intensities are practically flat. This result is an indication that at the distance of the grid, $z/h = 1$, where the measurements were made, the turbulence magnitudes are determined mainly by the mean shear and that the differences in scales introduced by the grid has been erased by the mean shear. This flatness of turbulence intensities was also found by other researchers (Borean et al., 1995; Rose, 1966; McCarthy, 1964).

For each point in the w and u measurements $N = 10{,}000$ data points were acquired. Thus, the statistical error for the mean velocities are $\Delta w = w_{\mathrm{rms}}/N^{1/2} = w_{\mathrm{rms}}/100$ and $\Delta u = u_{\mathrm{rms}}/N^{1/2} = u_{\mathrm{rms}}/100$, which in both cases are smaller than the size of the symbols in the plots.

Fig. 10 shows a gradual reduction of the linear slope as the z coordinate increases. It is

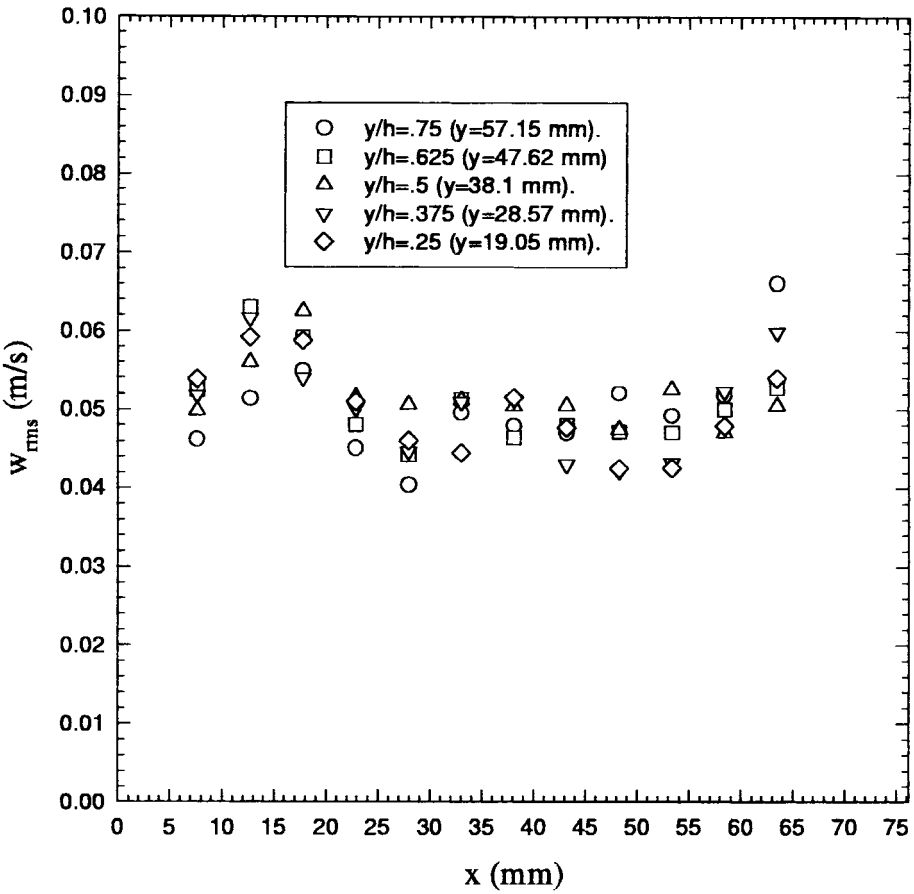

Fig. 7. Streamwise rms velocity at $z/h = 1$ for a centerline velocity of 0.56 m/s and at 55°C.

obvious from the figure that at $z/h = 2.16$ there has to exist a lateral movement of liquid form the high to the low velocity region. The figure corresponds to the highest flow rate used in this data set. Since with a reduction of flow rate the shear destruction region moves closer to the grid, it is clear that the $z = z_0$ plane where the lateral velocities are minimal is located for every flow rate at $z/h<2.16$.

The total area under each curve increases with z. This trend can be explained by the growth of the wall boundary layers that slows down the fluid entering them. Therefore, liquid in the core has to accelerate since the total flow rate was held constant.

4.1.2. Measurements at 26°C

Fig. 11 shows the velocity profiles at $z/h = 1$ and $y/h = 0.5$ at 26°C for different flow rates. As before, the mainstream velocity at the test section centerline was used to characterize flow rates. Unfortunately, the reduction of the Reynolds numbers of the channel and wires diminishes the grid performance, as is clear from the decrease in linearity visible in Fig. 11. However, a parabolic fit was sufficient to correct for non-linearities. Moreover, it will be seen

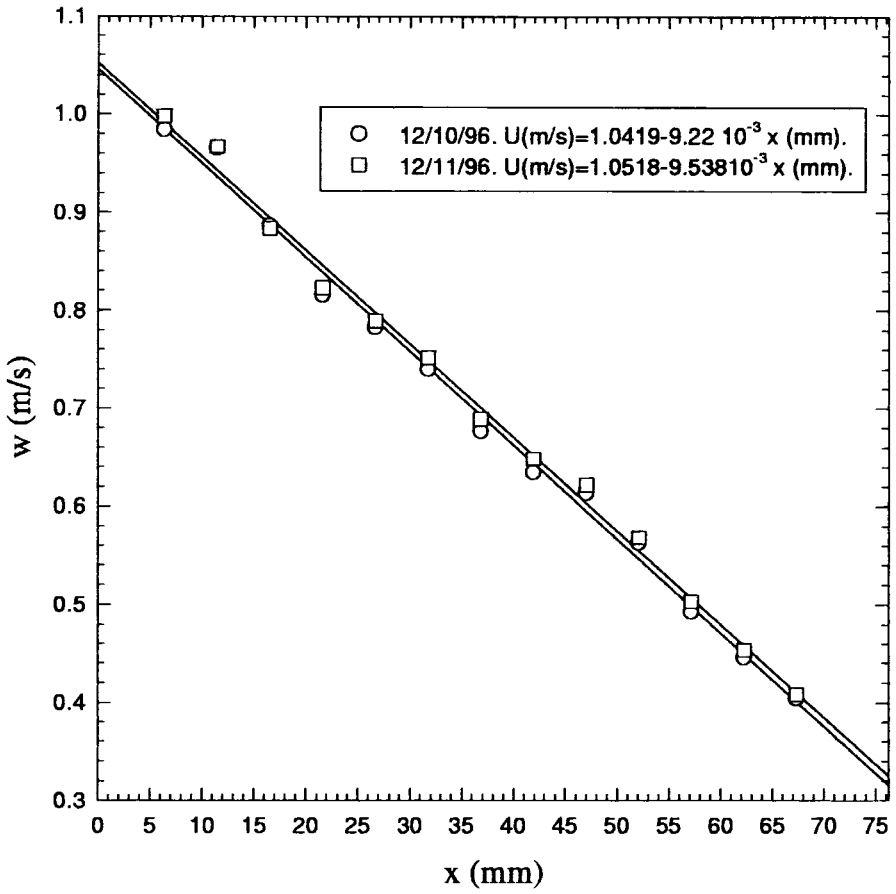

Fig. 8. Repeateability check of the streamwise velocity profile at $z/h = 1$.

in Section 6.2 that the range of movement in the x direction of the pendant is so small that we may safely neglect local departures from linearity. The parabolic fits were used to calculate the local vorticity, dw/dx, at $x/h = 0.34$ and 0.62 (or $x = 25.75$ and 47.0 mm, respectively). As will be seen in Section 6.2, the positions $x = 25.75$, 47.0 mm are of special relevance because they were selected as the hanging positions of the pendant. That is, when the pump was off and buoyancy was the only force acting on the sphere, the sphere center was located at these positions. Table 2 details the main parameters of these measurements, including the average mainstream velocity and vorticity at the above-mentioned positions. The local vorticity errors were calculated by propagation from the error of the coefficients of the fits. The average velocity errors were calculated using the already described procedure for the 55°C data. The standard deviation, σ, of the fits shown in Table 2 are smaller than the rms velocities. As was mentioned previously for the 55°C data, this fact is taken as an indication that from the point of view of the measurement of lateral forces on the pendant, the w velocity profiles were satisfactory. The high values of the square of the correlation coefficient, r^2, confirm this point of view.

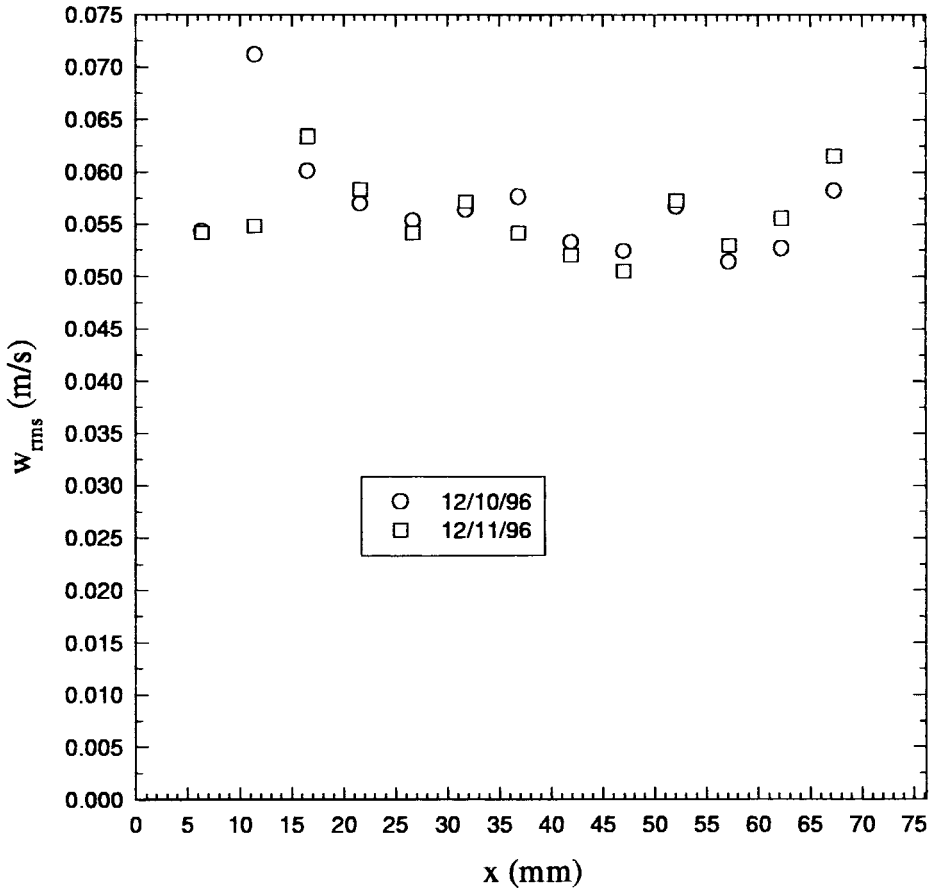

Fig. 9. Repeatability check of w_{rms} at $z/h = 1$.

Table 2
Streamwise velocity measurements at $z/h = 1$ and $y/h = 0.5$ at 26°C ($h = 76.2$ mm)

$w\|_{x/h=0.5}$ (1 ± 10^{-3}) m/s	$w\|_{x/h=0.34}$ (1 ± 10^{-3}) m/s	$w\|_{x/h=0.62}$ (1 ± 10^{-3}) m/s	$w_{\mathrm{rms}}\|_{x/h=0.5}$ $(10^{-3}$ m/s)	$\frac{\mathrm{d}w}{\mathrm{d}x}\|_{x/h=0.34}$ (1/s)	$\frac{\mathrm{d}w}{\mathrm{d}x}\|_{x/h=0.62}$ (1/s)	σ $(10^{-3}$ m/s)	r^2
0.085	0.095	0.079	5.7	0.9 ± 0.2	0.6 ± 0.3	2.4	0.978
0.119	0.132	0.113	5.4	1.3 ± 0.1	0.5 ± 0.1	1.3	0.995
0.175	0.189	0.167	9.5	1.3 ± 0.1	0.7 ± 0.2	1.8	0.993
0.228	0.247	0.219	8.4	1.9 ± 0.2	0.7 ± 0.3	2.9	0.990
0.270	0.294	0.259	12.4	2.3 ± 0.2	0.9 ± 0.2	2.0	0.997
0.326	0.356	0.310	11.5	2.8 ± 0.3	1.5 ± 0.4	3.7	0.993
0.450	0.527	0.403	31.8	7 ± 2	5 ± 2	19	0.976
0.477	0.558	0.427	33.8	7 ± 2	5 ± 2	22	0.972

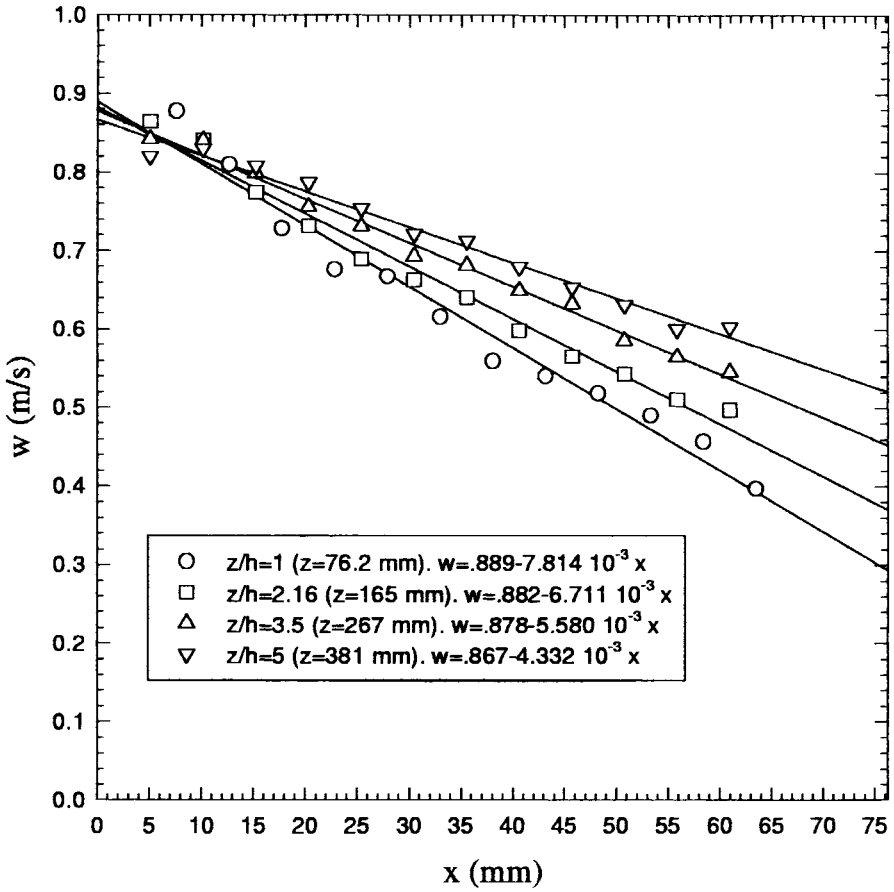

Fig. 10. Typical streamwise velocity profile variation along the test section at the centerplane $y/h = 0.5$. $w|_{x/h=0.5} = 0.67$ m/s.

For posterior reference a plot of the local relationship between the Reynolds numbers based on the local relative velocity (Re) and vorticity (Re_∇) is shown in Fig. 12 for a sphere of diameter $D = 12.7$ mm (1/2 in.). It is convenient to express the relationship between velocity and vorticity at a given position in term of Reynolds numbers to take into account the effect of the kinematic viscosity and its variation with temperature. The Reynolds numbers, Re and Re_∇, were varied independently changing the x rest position of the pendant, x_{rest}.

The flatness of the rms velocity profile seen in Fig. 13 indicates that in spite of the reduction of the channel Reynolds number, turbulent energy production by the shear remains the dominant factor determining the turbulent structure.

4.2. Lateral velocities, u

4.2.1. Finding the location of the minimum lateral velocities

Immediately after the grid, there exist a lateral velocity, $u<0$, that moves liquid toward the high velocity side. This movement is due to inertia and the creation of the velocity gradient by

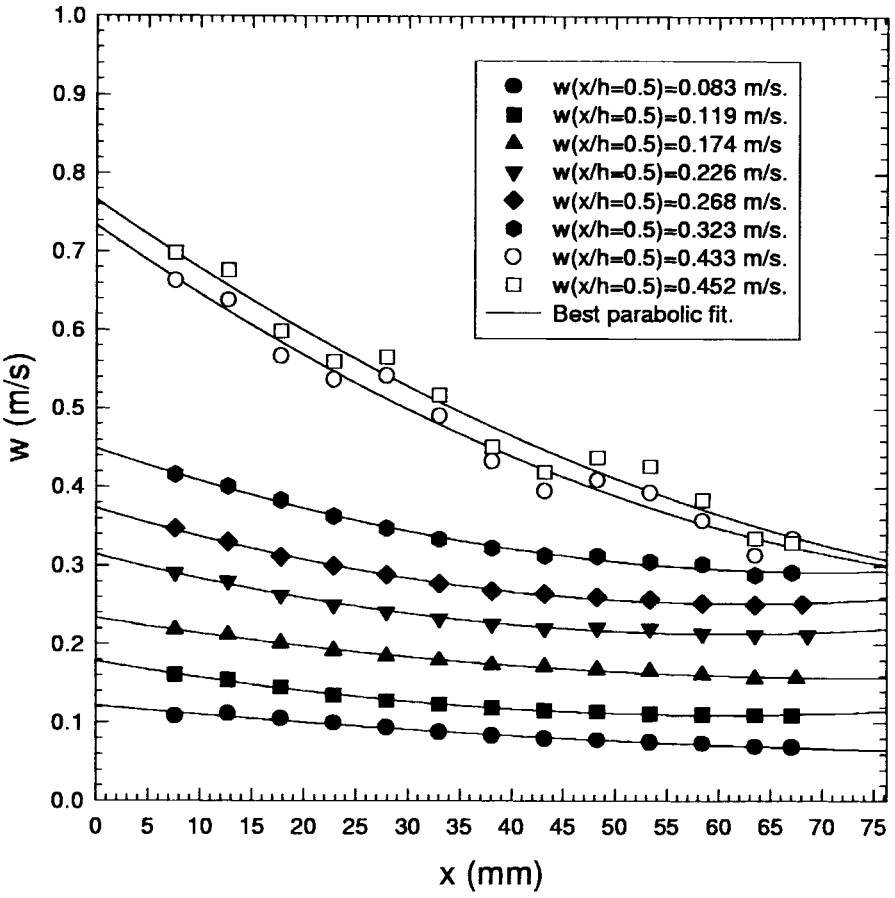

Fig. 11. Streamwise velocity profile at $z/h = 1$ and $y/h = 0.5$ at 26°C.

the grid. Far away from the grid, the destruction of the shear is associated with a flow toward the low velocity side ($u > 0$). In the transition region lateral velocities should be very small. This transition region is the place were the spheres should be placed to minimize lateral drag and make inviscid lift the dominant lateral force. For the purpose of this investigation, it is necessary to know accurately the lateral velocities only in this transition region, where the lateral forces will be measured. Thus, rather than make a complete mapping of the lateral force field at each position behind the grid, a mechanical method that helped determine where the minimum occurred was implemented. It is based on the realization that a flat plate hanging vertically in a x = constant plane will not experience any lateral force due to the average vorticity field, but it will be displaced by lateral drag forces. Therefore, the location where the plate was displaced the least from the vertical was the one having the minimal lateral forces. This method had the additional advantage of integrating the lateral velocity over the area of the plate which is considerably larger than the LDA measurement volume and of about the same size as most of the spheres used for the measurements.

Using a square stainless steel plate of 12 mm sides and 0.25 mm thick, it was determined

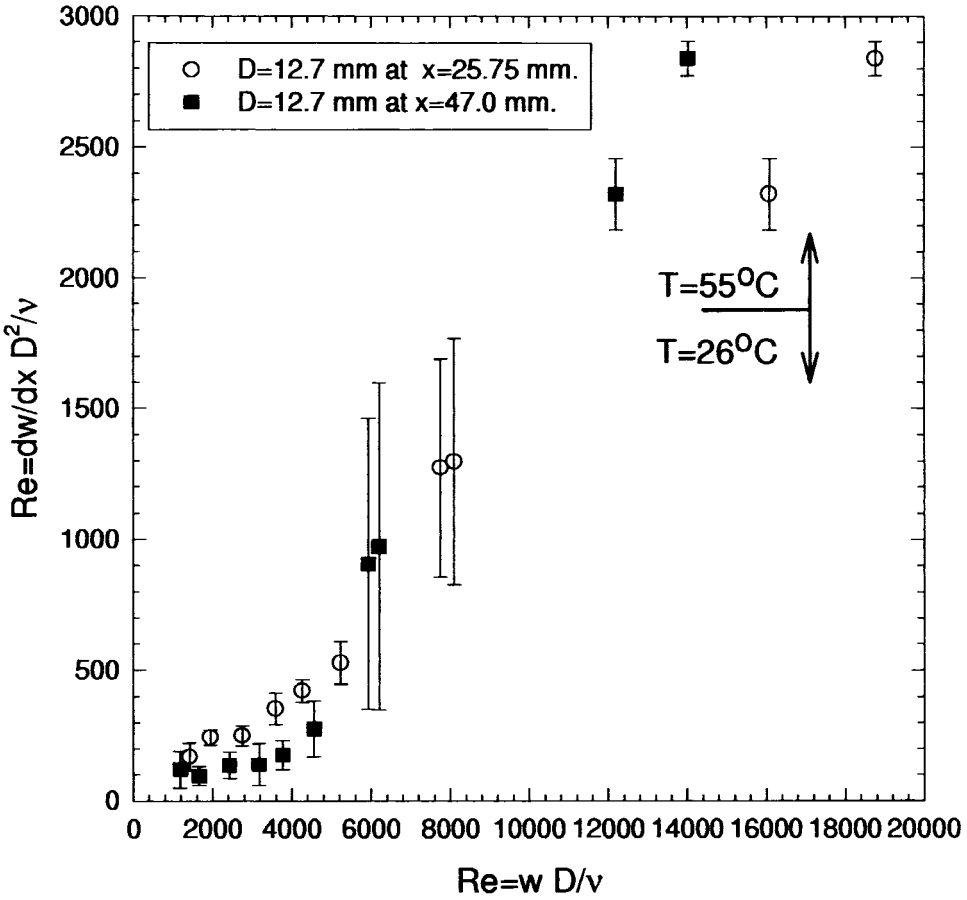

Fig. 12. Relationship between Reynolds numbers based on relative velocity (Re) and velocity gradient (Re_∇) for $D = 12.7$ mm at $x/h = 0.32$, 0.64, $y/h = 0.5$ and $z/h = 1$.

that the region where lateral forces were minimal corresponded to $z/h \leq 1$ (Moraga, 1998). This region was found to be rather insensitive to flow rate. The region where lateral forces are minimal should have a length of order h (Moraga, 1998). Given this length and the relative insensitivity of the method used to determine the position of this area, the independence of flow rate is to be expected. In order to take full advantage of the glass window placed at $z/h = 1$ to make LDA measurements, all lateral velocity measurements were made at this position. It will be seen from the results that at this horizontal plane the lateral velocities were low and varied little with system flow rate.

4.2.2. Measurements at 55°C

A small angle correction has to be introduced due to the large difference in magnitude of the u and w velocities. The corrected lateral velocity, u_c, is

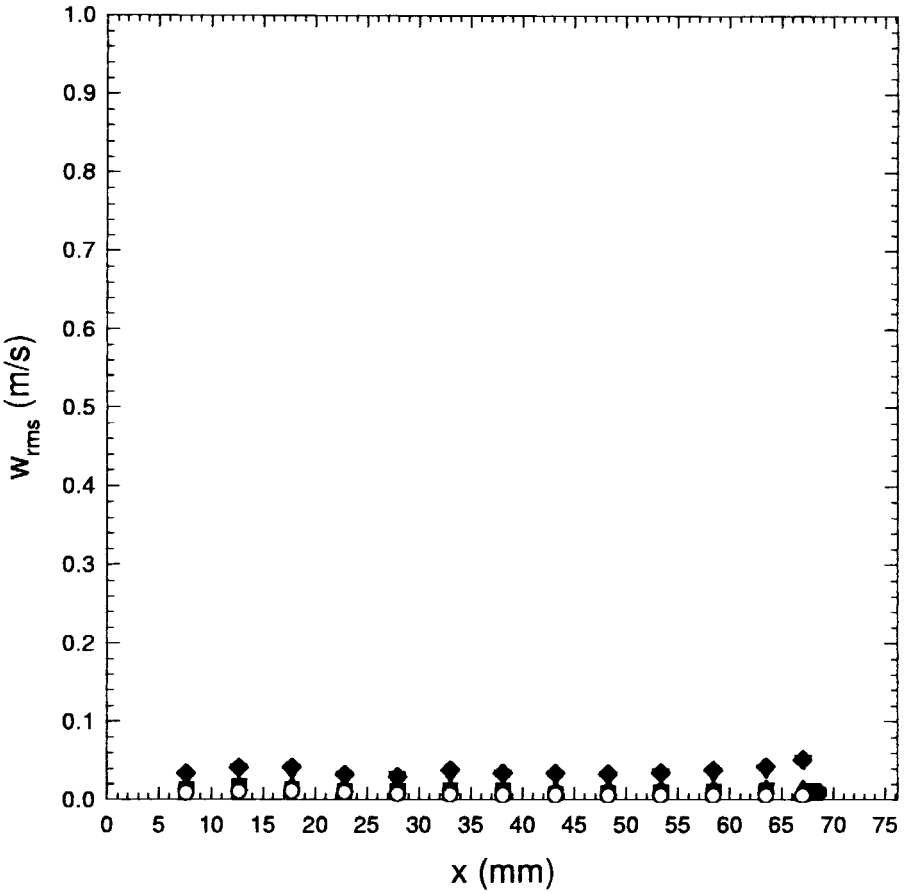

Fig. 13. Streamwise rms velocity profile at $z/h = 1$ and $y/h = 0.5$ at 26°C. For symbols detail see Fig. 11.

$$u_c = u + w\sin\left(\frac{0.5\pi}{180}\right) \tag{32}$$

For example, a centerline velocity of $w = 0.56$ m/s implies a correction $\Delta u = -5 \times 10^{-3}$ m/s. Lateral mean and rms velocities corresponding to the 0.56 m/s centerline velocity (Fig. 6) can be seen in Fig. 14. Both, the average and rms velocity profiles are rather flat with rms velocities being at least two times larger than the average velocities. As expected, the rms tends to increase with flow rate. They are also comparable in magnitude with w_{rms}, indicating a near isotropic turbulence structure. Moreover, since both, u_{rms} and w_{rms} are uniform in the x direction, no variations of the turbulence kinetic energy are expected in this direction. The statistical error of the lateral velocity measurements, u, was already noted above. It was found to be approximately 5×10^{-3} m/s, which is smaller than the symbol sizes in Fig. 14. The smallness of this error maked it necessary to consider the existence of other errors which are more difficult to quantify; electronic noise, for example.

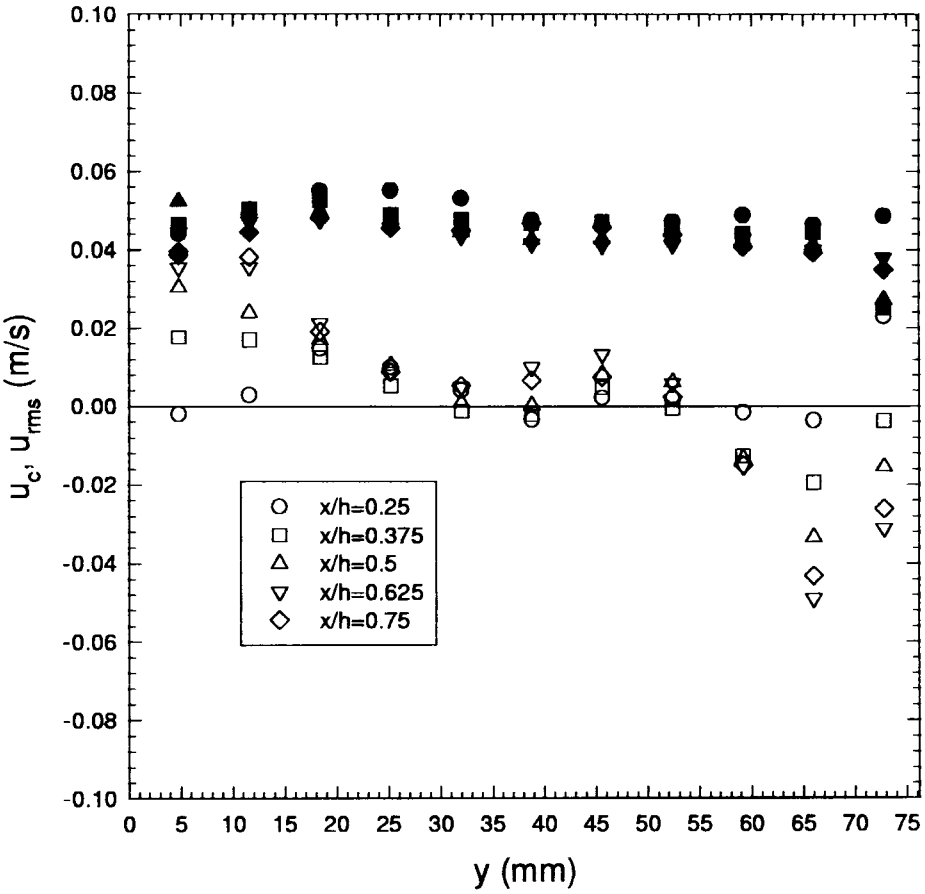

Fig. 14. Lateral average (open symbols) and rms (closed symbols) lateral velocity profile in the y direction at $z/h = 1$.

4.2.3. Measurements at 26°C

Fig. 15 shows the lateral average and root mean square velocity profiles at $z/h = 1$ and $y/h = 0.5$ for different centerline velocities. The comments already made for the 55°C lateral velocity measurements about the flatness of the rms profiles and the turbulent kinetic energy are applicable here too. Fig. 16 shows the variation with flow rates of the lateral velocities at $x/h = 0.34$ and 0.62. The lines in this last figure show the angle correction given by the second term in Eq. (32). Obviously, the magnitude of this correction tends to increase with the local value of w. Table 3 shows the already mentioned magnitudes and the root mean square velocities, which are several times larger than the absolute value of the average velocities.

5. Pendant experiments

This section describes the pendant and optical setups and the data acquisition and processing

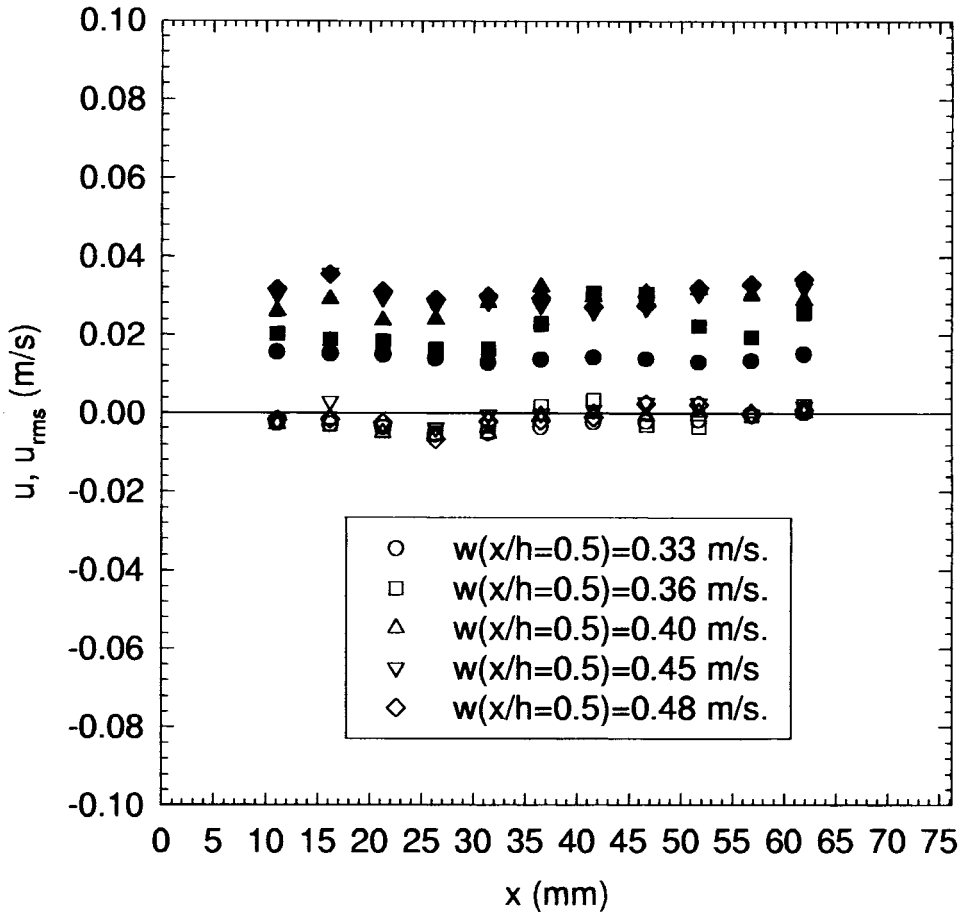

Fig. 15. Lateral average (open symbols) and rms (closed symbols) velocity profiles at $z/h = 1$ and $y/h = 0.5$ at 26°C for different centerline velocities.

Table 3
Lateral velocity measurements at $z/h = 1$ and $y/h = 0.5$ at 26°C ($h = 76.2$ mm)

$w\|_{x/h=0.5}$ (1 ± 10^{-3}) m/s	$u\|_{x/h=0.34}$ $(10^{-3}$ m/s)	$u\|_{x/h=0.62}$ $(10^{-3}$ m/s)	$u_{\mathrm{rms}}\|_{x/h=0.34}$ $(10^{-3}$ m/s)	$u_{\mathrm{rms}}\|_{x/h=0.62}$ $(10^{-3}$ m/s)
0.085	-4.4 ± 0.1	-15.8 ± 0.3	6	7
0.119	-4.6 ± 0.1	-14.0 ± 0.3	7	8
0.175	-4.4 ± 0.1	-14.0 ± 0.3	9	11
0.228	-4.9 ± 0.1	-6.9 ± 0.3	12	12
0.270	-4.1 ± 0.1	-7.0 ± 0.3	14	12
0.326	-5.4 ± 0.1	-2.2 ± 0.1	14	14
0.360	-5.1 ± 0.2	-3.1 ± 0.3	16	30
0.401	-5.6 ± 0.2	-7.6 ± 0.3	24	31
0.450	-3.8 ± 0.3	2.8 ± 0.3	27	27
0.477	-6.6 ± 0.3	2.4 ± 0.3	30	27

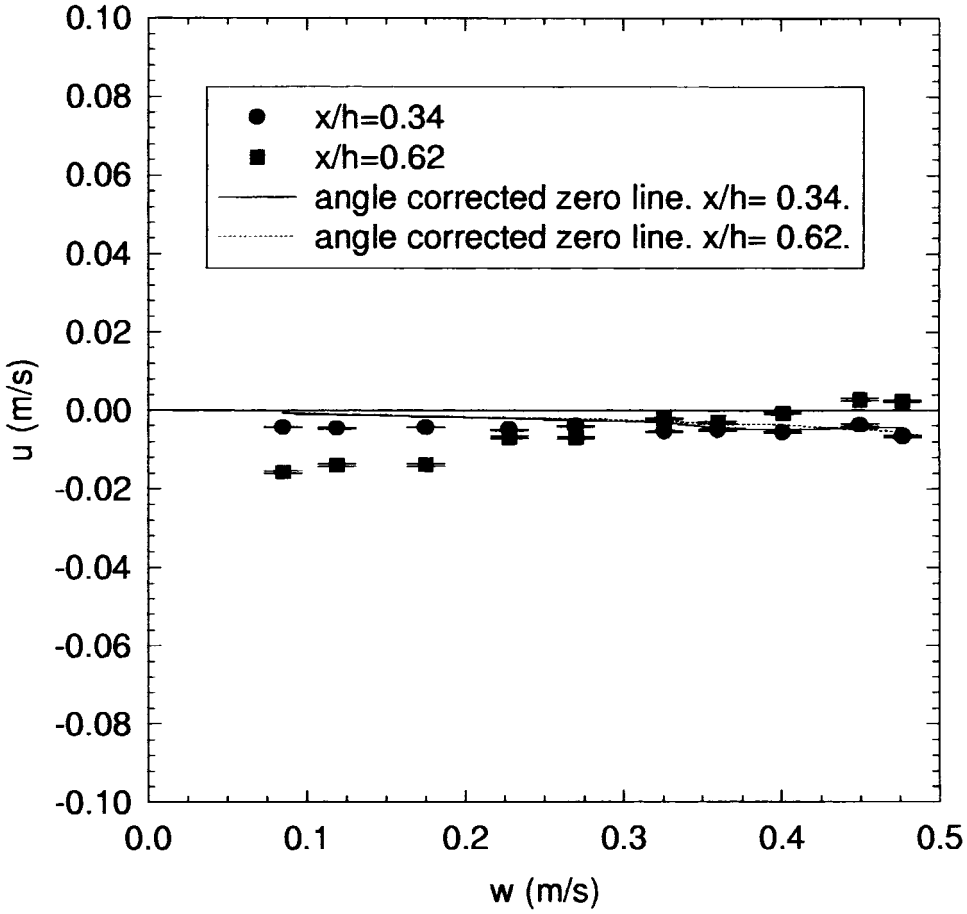

Fig. 16. Lateral, u, vs. centerline, $w|_{x/h=0.5}$, velocity at $x/h = 0.34$, 0.62, $z/h = 1$ and $y/h = 0.5$ at 26°C.

system. The experimental procedure and details of the consistency checks performed can be found elsewhere (Moraga, 1998).

5.1. Pendant setup

A schematic of the pendant and supporting structure can be seen in Fig. 17. The hanging point of the pendant was the tip of a stainless steel capillary tube of 1.27 and 0.84 mm OD and ID, respectively. This tube was shaped to minimize interference with the sphere movement in the x direction, the direction relevant for lateral forces. It was attached to a 6 mm diameter aluminum rod (not shown in Fig. 17) that could be moved to control the x position of the hanging point. On several occasions during the measurements it was verified that the capillary tube did not deform under the influence of drag and weight.

The pendant thread was a 0.15 mm diameter Spiderware™ microfilament line. This thread was selected for its small diameter, opaqueness and relatively well-defined contour, all important factors in determining the shape and duration of the pulses produced. In addition,

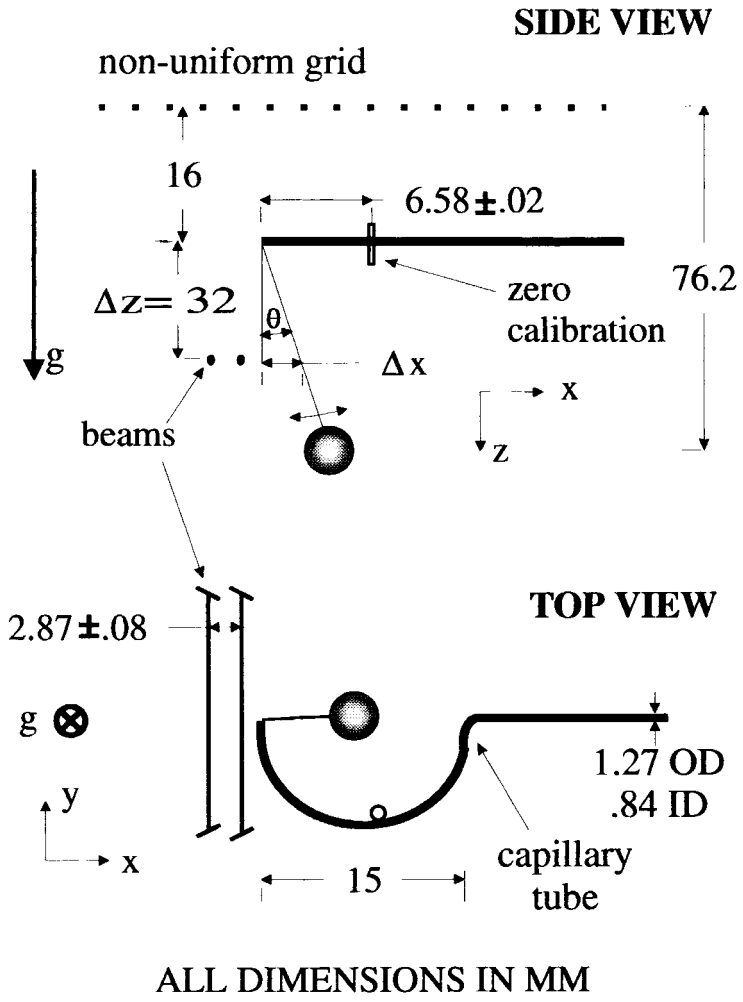

Fig. 17. Pendant schematic.

the thread has to always form a straight line between the hanging point and the spherical pendant. Otherwise a systematic error is introduced as the position of the sphere is inferred from that of the thread assuming that the latter is straight along all its length. It was found that this requirement is one of the key factors that sets a lower limit on the sphere Reynolds number at which experiments could be carried out, as particle drag and weight can become too small to keep the thread straight. For example, 6.35 mm diameter stainless steel spheres where too light and small to keep the thread straight at the lowest flowrate used. The thread selected required a smaller tension to adopt a straight profile than any other textile or plastic line tested. Another possible systematic error would arise if the sphere rotated around the point where it joins the thread. Fortunately, even at the largest amplitude of oscillations no rotation of this kind was observed.

After entering the capillary tube at the hanging point, the thread traveled through the tube a

Table 4
Properties of the spheres used[a]

Name	Material	Diameter, D (mm)	Weight (g)	Density, ρ_d (kg/m^3)
12.7ss	316SS	12.70	8.3 ± 0.1	7740 ± 90
9.52ss	316SS	9.52	3.5 ± 0.1	7750 ± 200
11.8p	Plastic	11.80 ± 0.05	0.99 ± 0.05	1150 ± 58

[a] Names are for future reference in tables.

distance large enough to ensure that it would not perturb the fluid motion in the neighborhood of the pendant. After leaving the capillary tube, the thread passed through a rubber seal.

Table 4 shows the properties of the spheres after the thread was attached to them. A groove 2 mm wide and about 2 mm deep was cut in each of the 316 stainless steel (SS) spheres. The thread and a small steel pin to which it was tied was inserted in the groove. The groove was filled with epoxy taking care to keep a spherical shape. Unavoidably the roughness of the stainless steel and epoxy surfaces were different. However, the grooves were small enough to be far from the boundary layer separation point and consequently they are not expected to influence the wake structure. Instead of a groove, a 1 mm diameter hole was filled with epoxy to attach the thread to the plastic spheres.

The blockage ratio, that is, the ratio of the sphere projected area to the test section cross-section area, was 2.2% for the largest sphere. Modi and Akutsu (1984) have shown that blockage effects on drag, the separation point of the boundary layer and the wake configuration are negligible for up to 11% in blockage. Thus, it is concluded that the wake structure was not affected by confinement effects.

A small nylon cylinder of 0.25 mm OD was glued to the capillary tube at a horizontal distance of 6.58 ± 0.02 mm. When a laser beam hit this cylinder, a light interference pattern arose. This pattern was used to determine the position of the hanging point and to ensure that it did not drift during the measurements. This method yielded a more accurate determination of the x position of the hanging point than possible measuring the hanging point position directly (Moraga, 1998).

5.2. Optical setup

A schematic of the optical setup is shown in Fig. 18. The beam produced by a 3 mW, 633 nm wavelength laser was collimated using a 252 mm focal length lens. This collimated beam was split into parallel beams using a mirror which was 5.92 ± 0.05 mm thick. Only the two more intense reflections were used. The distance between two consecutive beams was 2.87 ± 0.08 mm. To obtain this number the distance between the first and seventh mirror reflection was measured and divided by 6. This distance was measured several times to ensure that it did not changed over time. Repeatability within the range of the error bars was always obtained. The distance between beams was fixed by the physical size of the phototransistors

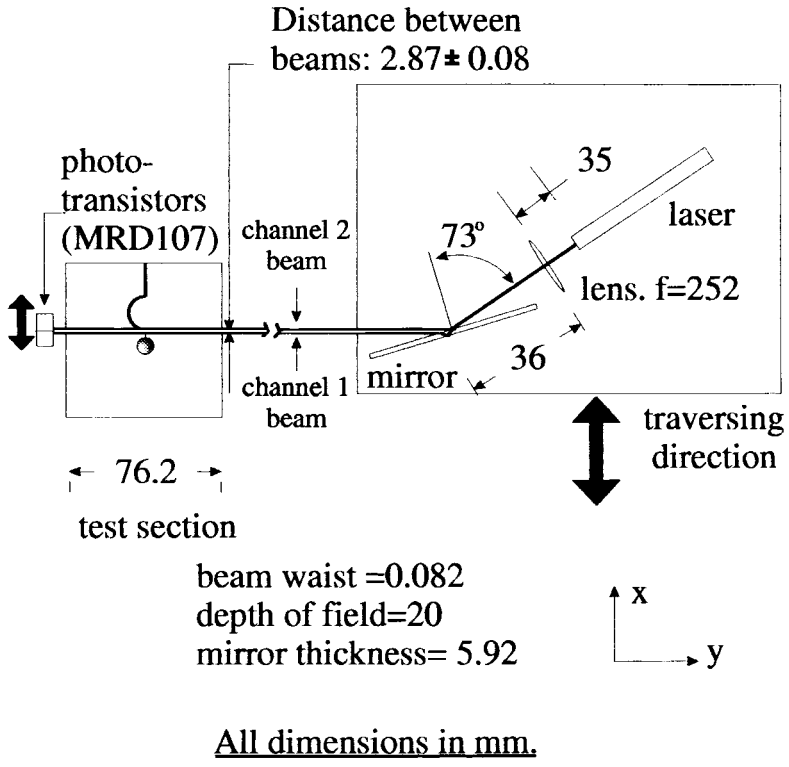

Fig. 18. Schematic of the optical setup.

and the need for having the beams hit the active areas of the phototransistors. Motorola MRD107 phototransistors were selected because they were the smallest phototransistors on the market at the time the experiments were performed.

The beams waist, 0.082 mm, and its depth of field, 20 mm, were calculated considering the diffraction limit (Saleh and Teich, 1991) and using geometric optics (Blaker, 1971) to account for the presence of the mirror. In this context the depth of field is defined as the axial distance within which the beam radius lies within a factor $\sqrt{2}$ of its minimum value (Saleh and Teich, 1991).

The horizontal phototransistor plane (see Fig. 17) was 48 mm below the non-uniform grid. Traversing the laser-lens-mirror set in the y direction, it was found that the laser beams were parallel to the y axis within a 0.37° angle. With a similar procedure it was found that the beams formed a 0.008° angle with the horizontal plane.

5.3. Data acquisition hardware and software

The data acquisition hardware that was used consisted of the already mentioned MRD107 Motorola phototransistors, an amplification stage and a PC data acquisition board that sent the signal to the selected PC interruptions. A digital oscilloscope with screen memory was

utilized to study the behavior of the circuit. The time resolution of the acquisition hardware was 0.084 ms. This number is the result of a calibration in which a square signal of constant and known frequency was acquired. Additional information on the data acquisition hardware and software and the experimental procedure can be found elsewhere (Moraga, 1998; Moraga et al., 1999).

5.4. Data processing algorithm

The main purpose of the processing algorithm was to determine the time fractions that the thread, and consequently the pendant, spent to the sides of the laser beams for any given position of the beams. These time fractions were then used to calculate the average position of the thread and consequently of the sphere. From this average position the average lateral force could be determined.

A second more easily achievable objective was to measure the velocity the pendant had going from one beam to the other. All data processing was performed by software after the data were acquired.

The time fractions can be estimated by using just the relative amount of pulses at each channel and ignoring the duration of the time intervals between pulses or, alternatively, using only the mentioned time intervals durations. Both possibilities were explored and they are discussed below.

5.4.1. Number of pulses algorithm

The fraction of the total measurement time that the thread is at a position $X > x$ can be estimated to be,

$$TF^N(X > x) = \frac{N_2}{N_1 + N_2}$$

where x is the middle point between the beams and N_1 and N_2 are the number of pulses acquired in channels 1 and 2, respectively. If x is so small that only pulses in channel 2 are acquired, $TF^N(X > x) = 1$, as expected. Similarly, if x is large enough so no pulses are acquired in channel 2, then $TF^N(X > x) = 0$. Since this estimator is not making use of all the information acquired, it should be expected to be relatively insensitive and consequently not the most appropriate algorithm to determine average positions. However, it has the advantage of being robust; that is, changes in the direction of movement of the thread while a beam is being interrupted will not introduce significant error. The other great advantage of this estimator is a lack of questionable supporting hypothesis. Thus, the results of other more elaborate algorithms can be compared to this one in order to assess their quality. More specifically, any algorithm that renders a time fraction functional dependance with x that:

1. is qualitatively very different than $TF^N(X > x)$ is likely not robust or based in a valid hypothesis.

2. has a smaller slope than $TF^N(X > x)$ in a neighborhood of $TF^N(X > x) = 0.5$ is more insensitive and should be discarded.

5.4.2. Position tracking algorithm

The only assumption necessary to track the sphere position with respect to the beams from the time sequence of beam interruptions is the following: each time a beam is interrupted the thread moves from one side to the other of the beam. Thus, if it is known that the thread was on the right of the beam at a given instant, after a beam interruption it will be on the left. The details of the implementation of an algorithm based on the just stated hypothesis can be found in the work of Moraga (1998) and Moraga et al. (1999). For the purpose of this exposition, it is sufficient to note the assignation rules in which the algorithm is based:

Rule 1: The time spent traveling from one beam to the other, that is, time intervals for which a pulse in a channel is followed by a pulse in the other channel, is split into two equal parts that are assigned to the left ($X<x$) and right ($X > x$) regions.

Rule 2: Time intervals delimited by two consecutive pulses in the same channel are assigned to the left region, for channel 1, or to the right region, for channel 2.

The symmetry of these rules clearly indicates that the boundary, x, between regions is the midpoint between beams. From now on, the x position of the beams will be specified by the x coordinate of the midpoint between beams. Finally, the fraction of the total measurement time that the thread is at a position $X > x$ is estimated as;

$$TF^{PT}(X > x) = \frac{ST_2 + ST_3/2}{ST_1 + ST_2 + ST_3} \tag{33}$$

where ST_i; $i = 1,2,3$, are the total times spent on the left of the channel 1 beam, on the right of the channel 2 beam and in between beams, respectively. They are calculated using rules 1 and 2 above.

The validation of the number of pulses and position tracking algorithms can be found elsewhere (Moraga, 1998; Moraga et al., 1999).

6. Experimental results

Two different types of pendant motion were observed, namely periodic and non-periodic. The parameters determining if a motion was periodic or not were flowrate, liquid temperature, position of the hanging point, sphere diameter and material. Within this parameter space, repeatability of the type of motion was observed. Because of their different dynamics these regimes needed separate consideration. This paper is concerned with the non-periodic regime, which is the most relevant for determining the lateral lift coefficient in multiphase flows. The periodic regime's data can be found elsewhere (Moraga, 1998; Moraga et al., 1999). Nevertheless, the very existence of a periodic regime is an indicator that lateral forces may be strongly influenced by vortex shedding.

6.1. Velocity histograms

Accurate velocity determination is possible only when two consecutive pulses occur in different channels. For any other intervals the distance traveled by the pendant is not known and consequently velocity determination is not possible. This limitation has two important effects. First, for a given x position of the beams the number of velocity measurements is much smaller than that of pulses acquired, and the histograms in this section do not show the complete lateral velocity distribution but that of the fluctuations large enough to interrupt one beam after the other. Moreover, as the distance from the average x position increases, the velocity of the pendant becomes smaller and on a proportionally smaller number of occasions two consecutive pulses occur in different channels. Thus, in order to ensure that the measured velocity distributions are statistically representative, the x position closer to the average is always chosen. This is the region where the results are more important since the main purpose of this histograms was to estimate the value of $\langle \frac{1}{\tau_D} \frac{d\theta}{dt} \rangle_{\theta=\theta_{eq}}$. The importance of this term was explained in Section 2.2.

Although the velocity of the thread, u_t, at the phototransistor's horizontal plane was the magnitude actually measured, the velocity of the sphere, u_d, can readily be obtained from the former as,

$$u_d = \frac{L}{r} u_t$$

where L and r are the radial distances from the hanging point to the sphere center of gravity and to the position of the beams, respectively. Because of the smallness of the angle, θ, formed between the vertical and the thread, the following approximation introduces negligible error,

$$r \simeq \Delta z$$

where Δz is the vertical distance between the hanging point and the photo-transistor plane.

Typical results for the 9.52 mm stainless steel sphere are shown in Fig. 19. The distributions shown have two peaks equidistant from the origin and are zero elsewhere.

The symmetry of the histograms suggest that the second term in $\langle \frac{d^2\theta}{dt^2} + \frac{1}{\tau_D} \frac{d\theta}{dt} \rangle_{\theta=\theta_{eq}}$ is small. More precisely, for the two positions surrounding x_{rest}, the tethered sphere x position in the absence of water flow, in Fig. 19(b) and (c), calculation of the relative error introduced by the large fluctuations velocity yields (see Eq. (22)),

$$\frac{\tau_v^2}{\tau_D} \frac{\left| \left\langle \frac{d\theta}{dt} \right\rangle_{\theta=\theta_{eq}} \right|}{\langle \tan \theta_{eq} \rangle_{\theta=\theta_{eq}}} < 6 \times 10^{-3}$$

where the absolute value of $\langle d\theta/dt \rangle_{\theta=\theta_{eq}}$ is used because the sign is different on the left and right of x_{rest}. The contribution of the average pendant velocity to the equilibrium position error is negligible compared with the statistical error arising from the time fraction fits. Unfortunately, because accelerations cannot be measured with just two beams, little can be said about the value of $\langle \frac{d^2\theta}{dt^2} \rangle_{\theta=\theta_{eq}}$. For that purpose three beams would be necessary.

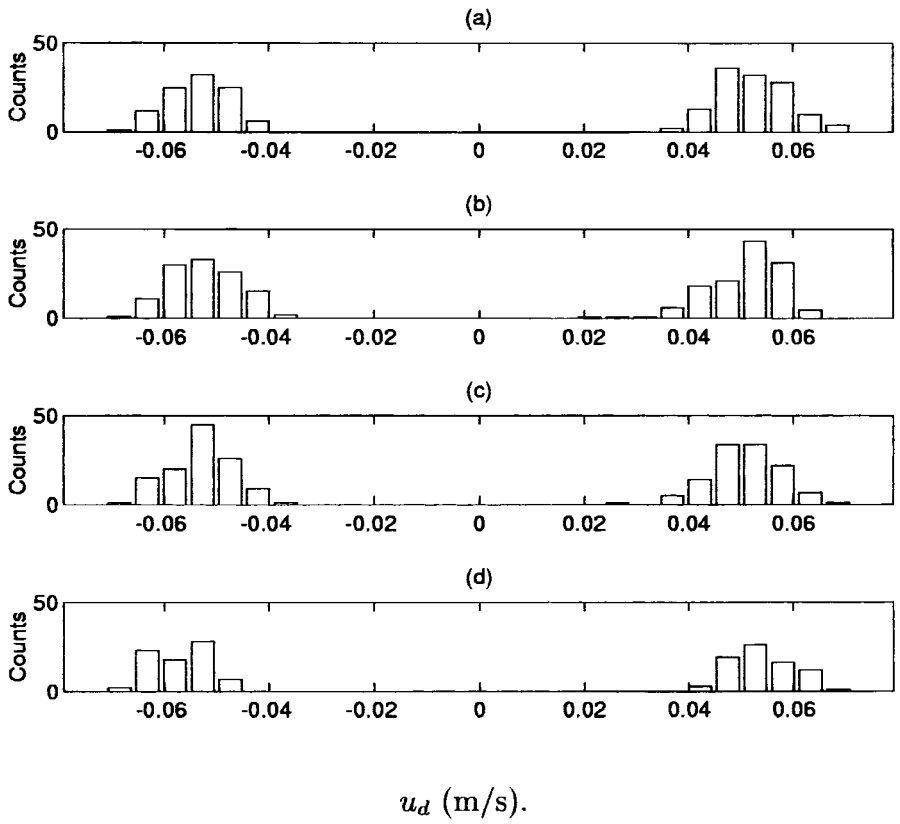

Fig. 19. Typical large uctuation lateral velocity distribution for non-periodic motion of a 9.52 mm stainless steel sphere at (a) $x = 46.89$ mm, $TF^{PT}(X > x) = 0.36$, (b) $x = 46.64$ mm, $TF^{PT}(X > x) = 0.47$, (c) $x = 46.39$ mm, $TF^{PT}(X > x) = 0.55$, and (d) $x = 46.13$ mm, $TF^{PT}(X > x) = 0.69$. $x_{\text{rest}} = 47$ mm at 26°C and $w|_{x/h=0.5} = 0.326$ m/s.

The lack of a continuum linking both peaks indicate that a minimum inertia is required to move from one beam to another passing through the equilibrium position. For x lower than the equilibrium position, the area under the positive peak is consistently larger than that under the negative one, and for x larger than the equilibrium position, the area order relation reverses. This pattern arise for all data sets. The areas under the peaks differ by as much as 50% far from the equilibrium position and become almost identical as the equilibrium position is approached.

6.2. Time fraction measurements

Typical profiles of the time fractions $TF^{PT}(X > x)$ and $TF^{N}(X > x)$ are shown in Fig. 20. For the particular case shown in the figure, $TF^{PT}(X > x)$ is negligibly steeper than $TF^{N}(X > x)$, although for other cases, the larger sensitivity of the position tracking algorithm was more evident. Assuming that the probability that the thread at the phototransistors plane (or the sphere at its horizontal plane) is at the interval $(x,x + \mathrm{d}x)$ obeys a Gaussian distribution, it can be shown that,

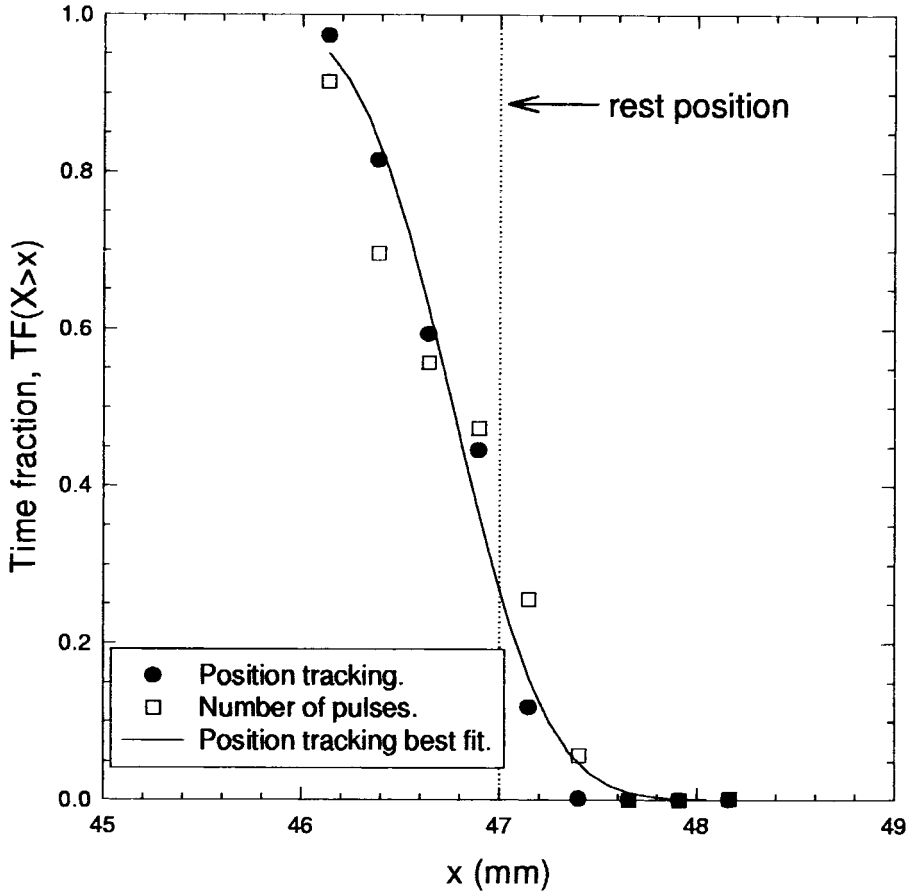

Fig. 20. Measured time fractions, $TF^{PT}(X > x)$ and $TF^{N}(X > x)$, for 9.52 mm stainless steel sphere, $x_{\text{rest}} = 47$ mm, $w|_{x/h=0.5} = 0.228$ m/s and 26°C.

$$TF(X > x) = \frac{1}{2}\left(1 - \text{erf}\left(\frac{x - x_0}{\sigma}\right)\right) \tag{34}$$

where x_0, σ and erf are the average value and the standard deviation of the Gaussian distribution and the error function, respectively. It must be noted that the hypothesis of a Gaussian spatial distribution ignores kinematic considerations. That is, information on speed and acceleration is ignored. Eq. (34) was used to determine x_0 and σ and the respective errors from the measured $TF^{PT}(X > x)$ through a non-linear fit using the Levenberg–Marquardt algorithm, as implemented in the Microcal™ Origin™ software package. The result of these fits are represented by the solid line in Fig. 20.

In order to make results independent of the value of x_{rest}, the average displacement, defined as,

$$\Delta x = x_0 - x_{\text{rest}}$$

was used instead of x_0 in Fig. 21. It must be stressed that because Re_{∇} is not explicitly stated,

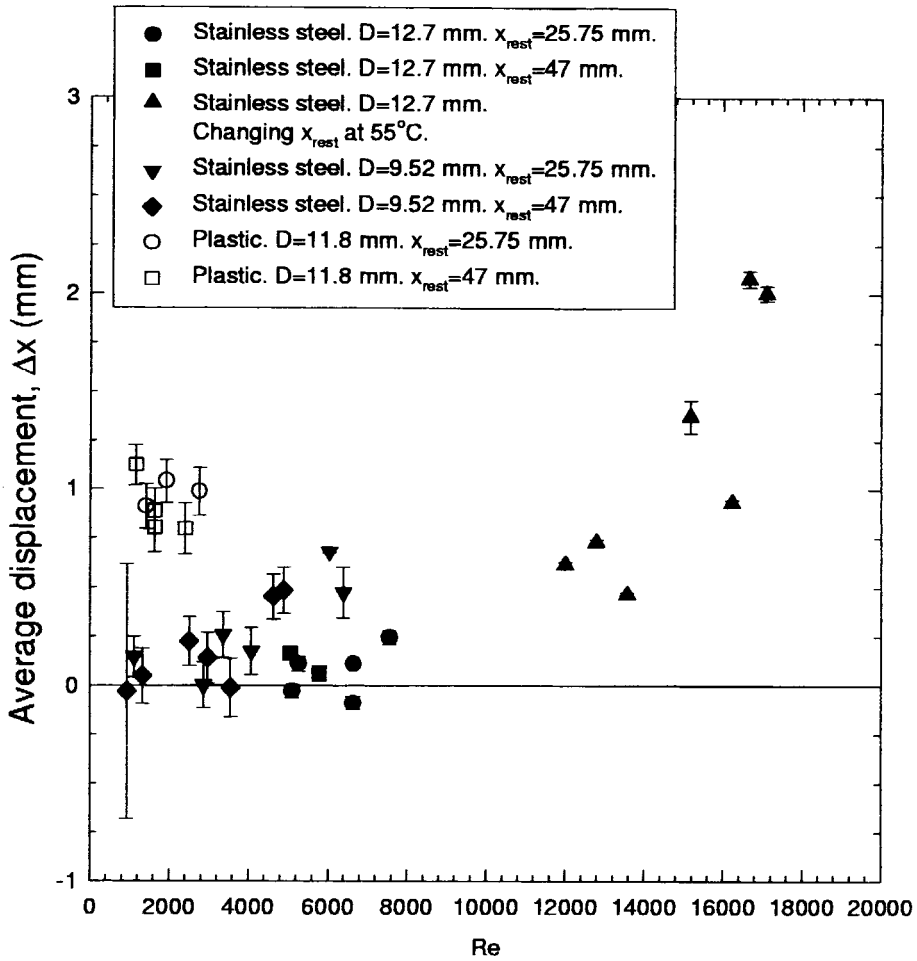

Fig. 21. Average displacement, $\Delta x = x_0 - x_{\text{rest}}$, vs. Reynolds number.

this plot is by itself incomplete, requiring the extra information of the relationship between both Reynolds numbers, which can be found in Fig. 12. It should also be noted that inviscid theory predicts, contrary to the results shown in Fig. 21, $\Delta x<0$. That is, inviscid lift should move the sphere toward the high velocity side. Moreover, because the plastic sphere was lighter, it can be more easily displaced from the vertical. This explains the consistently larger displacements, Δ_x, of the plastic sphere in Fig. 21.

The factor determining the minimum Reynolds numbers that can be used in this experiments is the minimum distance achievable between phototransistors, which in turn is determined by the phototransistors size. As the flowrate diminishes so does the amplitude of the oscillations. When this amplitude is so small that the laser beams are not interrupted often enough, the uncertainty of the measurements increases. That is the reason for the large error bar corresponding to the smallest *Re* in Fig. 21.

6.3. Force measurements

Force determination was based on a static force balance that relates the average departure from the vertical position, Δx; determined in Section 6.2, to the lateral force due to the uniform velocity gradient. As was seen in Section 2.2, the implicit hypothesis is that at the equilibrium position determined by Δx, time averaging of the instantaneous forces will cancel out any instantaneous fluctuations and leave only the net effect of the lateral forces.

From Fig. 17, and a balance of forces in the horizontal and vertical directions, the non-drag lateral force on the sphere is,

$$\begin{matrix}\textit{Lateral}\\ \textit{Force}\end{matrix} = \left(\frac{\pi}{6}D^3(\rho_d-\rho)g + \frac{\pi}{8}C_D D^2\rho\sqrt{w^2+u^2}w\right)\frac{\Delta x}{\Delta z} - \frac{\pi}{8}C_D D^2\rho\sqrt{w^2+u^2}u \tag{35}$$

where the parenthesis in the first term represents the sum of buoyancy and vertical drag and the second term is the drag in the horizontal direction. The drag coefficient, C_D, is calculated taking into account the absolute value, $\sqrt{w^2+u^2}$, of the liquid velocity. The total drag is then projected in the vertical and horizontal directions to obtain the corresponding components in Eq. (35). It should be stressed that $u \ll w$, thus the error introduced if the drag coefficient were calculated using the absolute value of w only, would not be large. Yet, it is necessary to introduce a lateral drag correction to make sure that the lateral forces are due to the local dw/dx and not to the u velocity. All the velocities in Eq. (35) were evaluated at (x_{rest},$y = 38.1$ mm, $z = 76.2$ mm). The smallness of Δx and the smooth variation of the velocity field makes the error introduced by evaluating velocities at x_{rest} of the order of 1% of this velocity. This small variation will have negligible impact on the lateral force error compared with the Δx error.

The drag coefficient was evaluated using the standard drag curve for sphere submerged in an uniform flow as recommended by Clift et al. (1978), which, in the range of interest for this work, is:

$$C_D = \begin{cases} 10^{(1.6435-1.1242r+.1558r^2)} & 2.6\times10^2<Re<1.5\times10^3 \\ 10^{(-2.4571+2.5558r-.9295r^2+.1049r^3)} & 1.5\times10^3<Re<1.2\times10^4 \\ 10^{(-1.9181+.6370r-.0636r^2)} & 1.2\times10^4<Re<4.4\times10^4 \end{cases} \tag{36}$$

where

$$r = \log_{10}(Re)$$

According to Eq. (36), C_D varies smoothly and continuously between approximately 0.45 and 0.40. Yamamoto et al. (1993) measured drag coefficients in a uniform shear flow for Reynolds numbers ranging between 1.2×10^4 and 3.8×10^4. These researchers found that the average drag coefficient for different values of the shear was $C_D = 0.46\pm0.03$, in good agreement with the standard drag curve. The drag measurements of Yamamoto et al. (1993) were conducted downstream of a grid similar to ours, with a 5% turbulence intensity, while our measurements are for a 8% turbulence intensity. Given the similarities in the grids and turbulence intensities between this work and that of Yamamoto et al. (1993) the standard drag curve should be

applicable to our measurements. Dandy and Dwyer (1990) have shown that C_D is insensitive to shear for Reynolds numbers up to 100. Clift et al. (1978) report that C_D is rather insensitive to particle spin from Reynolds numbers between 4.6×10^4 and 1.1×10^5. The comparison is appropriate because particle spin is expected to distort the shape and position of the wake in forms similar to that of shear. From the work of all these researchers it was concluded that it was reasonable to use the standard drag data for uniform flows to calculate drag in a shearflow.

The measured lateral force as a function of the Reynolds number can be seen in Fig. 22. Comparison with Fig. 21 shows that the data for plastic spheres tend to collapse with those of

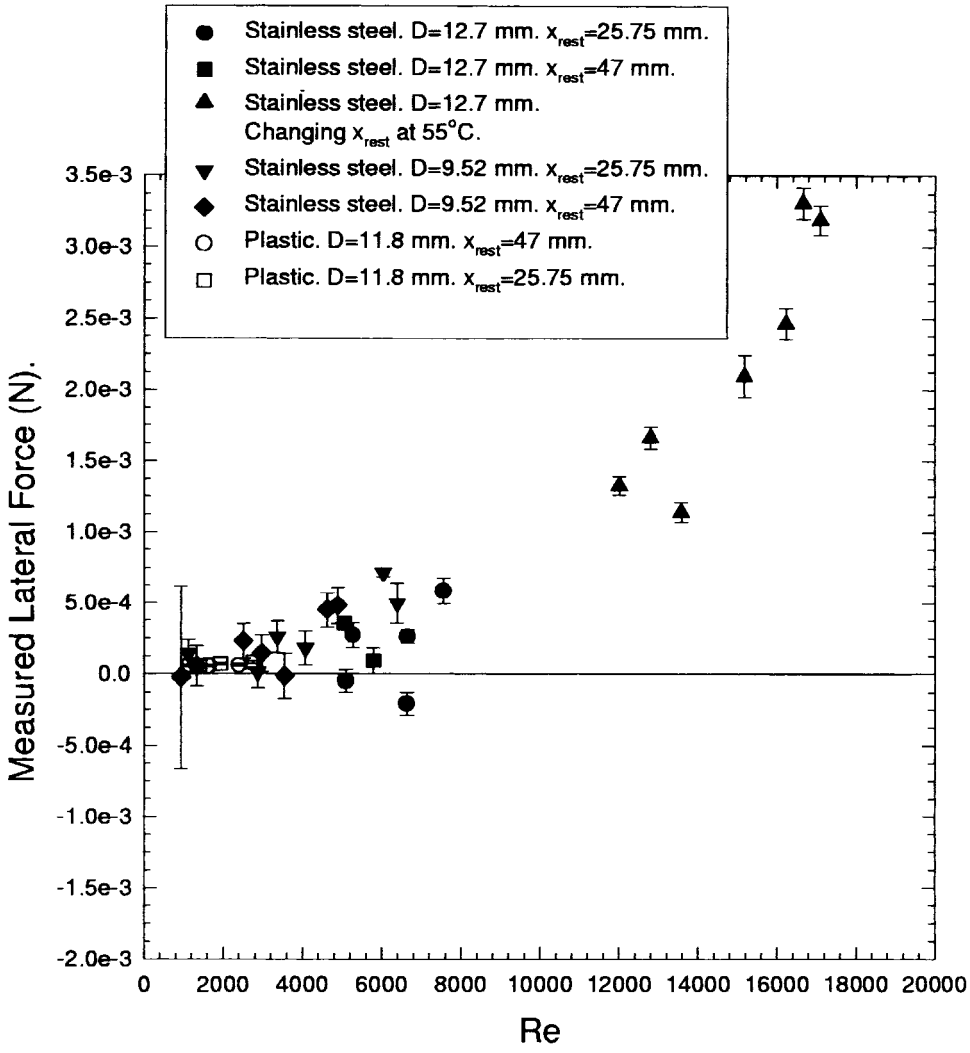

Fig. 22. Measured lateral force vs. Reynolds number.

Table 5
Lateral-drag/total-lateral-force ratio

Sphere	x_{rest} (mm)	$\frac{\text{lateral drag}}{\text{total lateral force}}$ (%)
9.52ss	47	−25 to 25
9.52ss	25.75	−5 to 1
12.7ss	25.75, 47	−5 to 10
12.7ss	several x_{rest} at 55°C	1 to 5
11.8p	25.75, 47	−20 to −15

steel for similar Reynolds numbers. This is because plastic is lighter, thus the same lateral force pushes the equilibrium position of plastic spheres further away form the vertical.

The magnitude of the lateral drag correction deserves special attention. The ratio of the lateral drag correction (i.e., the second term in Eq. (35)) and the total lateral force is detailed in Table 5. It ranged from −25 to 25%, but for some sets of data it varied, in absolute value, between 1 and 5%. There were only two data points that did not fit in the ±25% range because the total lateral force was small. These two points were not considered representative because the first and second term in Eq. (35) had different signs but similar magnitudes. Nevertheless, this brings out another important fact about the lateral drag correction. Since the sign of u_c velocity was positive or negative depending on x_{rest}, the lateral drag correction could be either negative or positive. For the particular case of $u_c<0$ the correction has the same direction as the inviscid lift force. Thus, this correction tended to enhance inviscid lift effects.

The sources of error considered for the error calculation were those associated with u, w and Δx. The error of the vertical velocity was statistical in nature and was conservatively set as $\Delta w = 7 \times 10^{-4}$ m/s (see Table 2). This number correspond to the largest observed error of the average velocity w at the sphere rest positions considered. The error of the lateral liquid velocity was calculated as $\Delta u = 4.9 \times 10^4 + \sin(0.2\pi = 180)w$; where the first term is a conservative value for the statistical error in the determination of u and the second takes into account the error, $\pm 0.2^\circ$, in the measurement of the angle the test section formed with the vertical.

The error of Δx was obtained from the time fraction fits. For most of the cases the Δx error accounts for more than 90% of the total force error. The exception being the measurements at 55°C, for which the Δx error ranged from 20 to 40% of the total. Practically all of the remaining lateral force error came from that of u, since the relative importance of the w error was negligibly small with respect to that of u and Δx. It is worth noting that velocity gradient errors are not relevant for the determination of the lateral force, but rather for the lift coefficient.

7. Data analysis

The most striking feature of the present data is that for most cases the lateral force on the spheres has the opposite sign to that predicted by inviscid theory, and thus, these data differ from those of all other researchers, with the exception of Yamamoto et al. (1993). Unlike the

study of Yamamoto et al. (1993), this discrepancy cannot be attributed to lateral drag. It should be recalled that the lateral drag correction introduced into the force determination represented a percentage of the total force too small to be responsible of a change of sign (see Table 5). Moreover, for some data points the lateral drag correction was in the direction predicted by inviscid theory.

The sign reversal has been discussed in Section 2.1 on the ground of vortex shedding and wake asymmetries being dominant over the traditional inertia effects expected in a configuration without boundary layer separation. That is, if the Reynolds number were reduced, a change of sign would be found as vortex shedding becomes less important. In the remaining part of this section it will be shown that many facts support this point of view.

It has been shown in Section 2.1 that wake effects on lift should have the same functional dependance as inviscid lift. Hence, it is appealing to fit the data using a non-dimensional form of that functional dependance (see (6)),

$$\frac{\text{Measured lateral force}}{\pi v^2 \rho/6} = C_{\mathrm{LT}} Re\, Re_{\nabla} \tag{37}$$

where $C_{\mathrm{LT}} = C_{\mathrm{LT}}(Re\, Re_{\nabla})$ is the total (inviscid and wake effects) lift coefficient which depends only on the product $Re\, Re_{\nabla}$, and is given by:

$$C_{\mathrm{LT}} = C_{\mathrm{L0}} \exp\left(\frac{Re\, Re_{\nabla}}{(Re\, Re_{\nabla})_0}\right) \tag{38}$$

where C_{L0} is the value of the lift coefficients at small values of the product $Re\, Re_{\nabla}$ and $(Re\, Re_{\nabla})_0$ represents a lower bound of the region for which C_{LT} is much larger than C_{L0}. The result of a non-linear fit to Eqs. (37) and (38), with error bars as weighting factors and utilizing the Levenberg–Marquardt algorithm as implemented in the Microcal™ Origin™ software yields for the high Reynolds number data presented herein:

$$C_{\mathrm{L0}} = 0.17 \pm 0.04 \tag{39}$$

$$(Re\, Re_{\nabla})0 = (4.2 \pm 0.1)10^7 \tag{40}$$

It can be seen in Fig. 23 that this fit follows the data very closely. Perhaps its only drawback is that it is not suitable for extrapolation to values of $Re\, Re_{\nabla}$ below the measured range, and as a consequence it does not predict the expected change of sign as the product of the Reynolds numbers diminishes. It must also be remembered that for the shear flow used in this work, the turbulence length scales are small with respect to the particle size. Thus, the fit given by Eqs. (37)–(40) is strictly valid only when turbulent length scales are small compared with the particle size.

Let us next consider extending Eq. (37) to the lower Reynolds numbers.

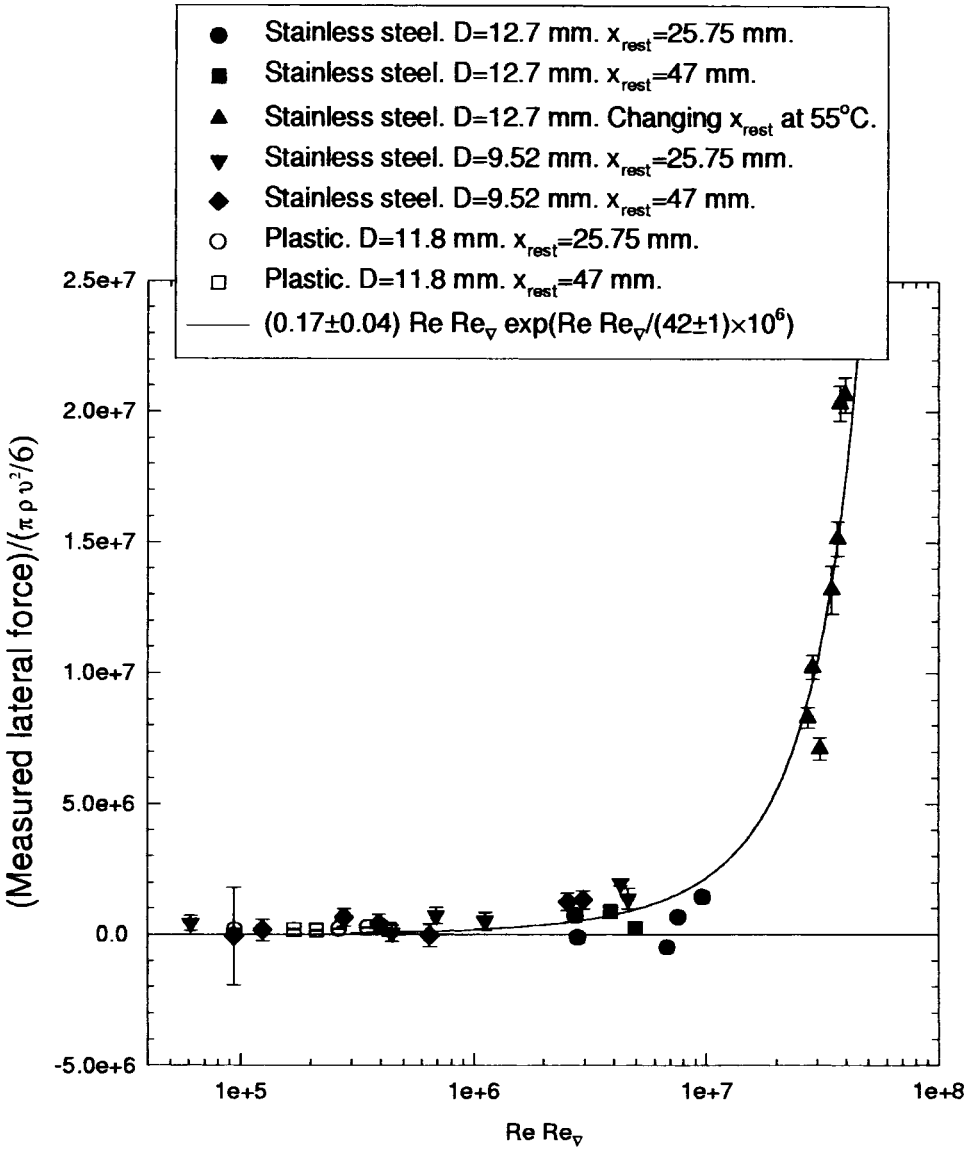

Fig. 23. Fit of measured lateral force vs. the product $Re\,Re_{\nabla}$.

8. Comparison with other researchers work

8.1. Solid particles at high $Re\,Re_{\nabla}$

The data of Yamamoto et al. (1993), acquired using three different grids also correlate with the product $Re\,Re_{\nabla}$. However, Yamamoto et al. (1993) measured somewhat larger lift coefficients than those obtained in the present work. Very probably the difference is due to the fact that Yamamoto et al. (1993) did not introduce a correction for lateral drag. Since they did

not measured the lateral velocities it is not possible to quantify the systematic error that was introduced. However, the fact that similar lift coefficients were obtained by Yamamoto et al. (1993) for free falling spheres and pendants at a fixed distance from the grid, suggest that the value of the correction introduced by drag is relatively small.

Turbulent uniform shear flows are quasi-self-sustained (Owen and Zienkiewicz, 1957; Moraga, 1998). This has been found to be particularly true in air loops, as the used by Yamamoto et al. (1993, 1995). Thus, it is not so surprising that the lateral drag experienced by a particle traveling downstream of the grid is small and relatively independent of the distance to the grid.

8.2. Solid particles at intermediate $Re\ Re_\nabla$

Alajbegović (1994) and Alajbegović et al. (1994) fitted lift coefficients applying the two-fluid model to experimental data of solid spheres submerged in a fluid moving upwards in a vertical pipe. It was found that $C_L = -0.15$ and -0.01 for ceramic and expanded polystyrene particles, respectively. The minus sign indicates that the lift force found by Alajbegović (1994) and Alajbegović et al. (1994) is in the direction predicted by inviscid lift. The good agreement between the experimental results and the simulations with the two-fluid model, which models the lateral force using a traditional inviscid lift formulation, suggest that in the range of relative velocities and shear investigated by Alajbegović, lift forces follow the inviscid lift functional dependance. However, just one value of the lift coefficient was used for the whole range of the product $Re\ R_\nabla$, which varied between zero at the pipe's center line and 10^6 close to the wall. Nevertheless, these data imply that the cross sectional average lift coefficient is $C_L = -(0.08 \pm 0.04)$. This value of C_L, and its error, are in agreement with that reported in the literature for fully developed bubbly flow in a pipe (Wang, 1986; Wang et al., 1986; Lahey et al., 1993).

As it was explained in Section 6.2, measurements were not carried out for $Re < 1000$, since the experimental uncertainty was too large in this region. However, extrapolation for smaller values of the product $Re\ Re_\nabla$ is desirable to study consistency with the inviscid lift formulation as implemented in two-fluid models. Hence, in order to make a fit combining the pipe flow data and those of the present work the following correlation is recommended:

$$\frac{\text{Lateral force}}{\pi\rho\nu^2/6} = \left[C_{L0} - \Delta C_L \exp\left(-\frac{Re\ Re_\nabla}{(Re\ Re_\nabla)_1}\right)\right]\exp\left(\frac{Re\ Re_\nabla}{(Re\ Re_\nabla)_0}\right) Re\ Re_\nabla \tag{41}$$

For $\Delta C_L = 0$ the expression successfully used to fit the experimental data measured in this study is recovered. The ΔC_L term is necessary to model the dominance of inviscid lift over wake effects at low values of $Re\ Re_\nabla$. Note that $C_{L0} - \Delta C_L$ is the value of the lift coefficient for $Re\ Re_\nabla \ll (Re\ Re_\nabla)_1$. The parameter $(Re\ Re_\nabla)_1$ is related to the critical $Re\ Re_\nabla$ for which the total lateral force is zero.

The resulting fit can be seen in Table 6 and in Fig. 24. This correlation for the lift force coefficient may be used in two-fluid models. It can be noted that not only is the lift coefficient practically constant, and close to the desired value at the lower range of $Re\ Re_\nabla$, but also the zero lateral force product of Reynolds numbers has increased to $(Re\ Re_\nabla)_{\text{zero lift}} = 2.2 \times 10^5$,

Table 6
Best fit of this study's data and that of Alajbegović et al. (1994). The last column indicates the value of $Re\,Re_{\nabla}$ for which the total lateral force is zero

$(Re\,Re_{\nabla})_0\ 10^7$	C_{L0}	$(Re\,Re_{\nabla})_1\ 10^4$	ΔC_L	$(Re\,Re_{\nabla})_{\text{zero lift}}\ 10^4$
3.0 ± 0.7	0.12 ± 0.03	36 ± 400	0.2 ± 0.2	22

which corresponds to a pipe radius of $r/R \approx 0.9$, a value more consistent with the observed wall peaking in upwards fully developed flow. Therefore, the recommended fit of the total lift coefficient, valid in the range $6 \times 10^3 \leq Re\,Re_{\nabla} < 5 \times 10^7$, is:

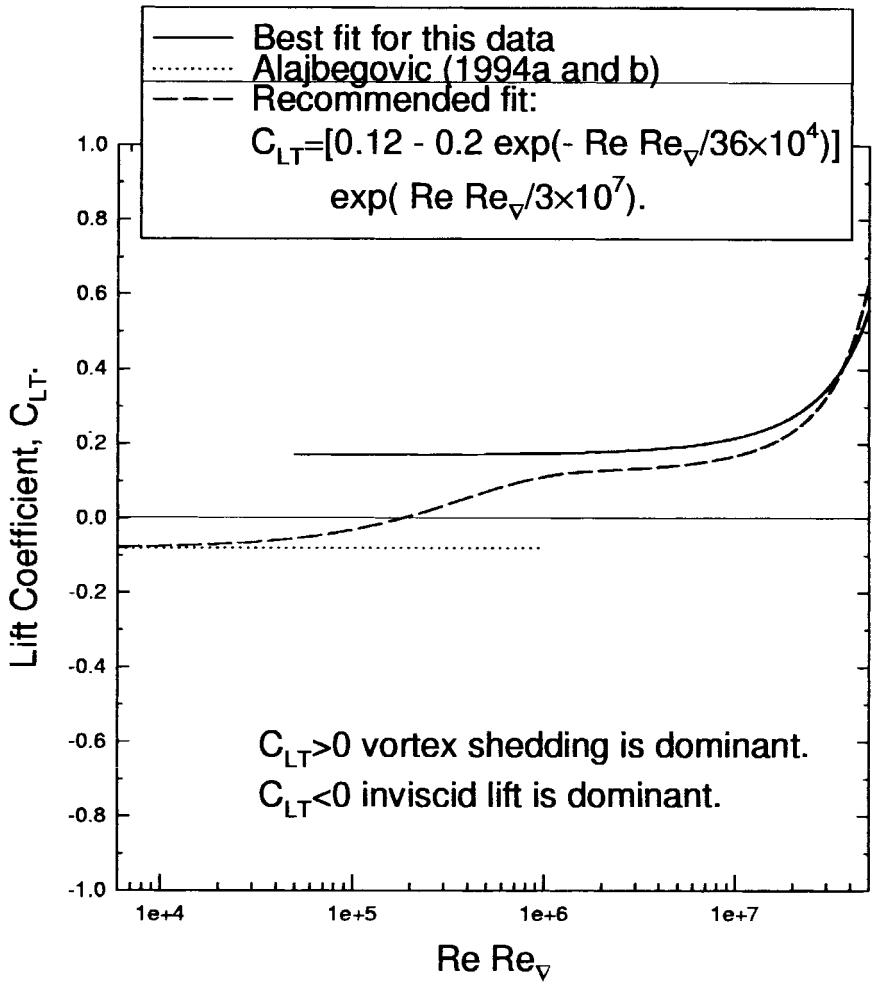

Fig. 24. Lift coefficients best fit to the data in this study and the data of Alajbegović et al. (1994).

$$C_{LT} = \left[C_{L0} - \Delta C_L \exp\left(- \frac{Re\ Re_\nabla}{(Re\ Re_\nabla)_1} \right) \right] \exp\left(\frac{Re\ Re_\nabla}{(Re\ Re_\nabla)_0} \right) \tag{42}$$

where the coefficient values can be obtained from Table 6. The large relative error of $(Re\ Re_\nabla)_1$ is due to the fact that the recommended fit is an interpolation since there are no data in the intermediate range $6 \times 10^4 < Re\ Re_\nabla < 1 \times 10^6$. It must also be remembered that the recommended fit is only valid for flows with characteristic turbulence length scales smaller then the particle size.

8.3. Solid particles at low Re Re_∇

There are many determinations of the lift coefficient in the bubbly two-phase flow literature. However, in very few instances are the data sets complete enough to rearrange them to a form appropriate for comparison with this work. One of the experimental works that allows comparison is that of Eichhorn and Small (1964), who measured lift forces on solid spheres submerged in a Poiseuille flow for Re and Re_∇ ranging from 80 to 250 and 0 to 360, respectively. These researchers levitated spheres in an inclined tube through the balance of buoyancy, drag and lateral forces. As was done by many other authors, they defined the lift coefficient by analogy with the drag coefficient,

$$C_{Laero} = \frac{\text{Measured lateral force}}{\frac{\pi}{8}\rho D^2 w^2}, \tag{43}$$

which is related to the lift coefficient measured in this work by the relation,

$$C_{LT} = \frac{3Re}{4Re_\nabla} C_{Laero} \tag{44}$$

Dandy and Dwyer (1990) calculated lift coefficients as defined in Eq. (43) for Re and Re_∇ up to 100 and 16, respectively. The upper bound of the Reynolds number was set to avoid boundary layer separation. Thus, no wake effects are present in the results of Dandy and Dwyer. The works of Eichhorn and Small (1964) and Dandy and Dwyer (1990) indicate that the lift coefficient is not a function of the product $Re\ Re_\nabla$ for $Re < 250$. This is attributed to the Reynolds number being too small for the hypothesis of inviscid theory to be valid. Finally, Mei (1992) was able to correlate the data of Dandy and Dwyer (1990) with the non-dimensional numbers, Re and $\alpha = Re_\nabla^{1/2}/Re$, using the functional dependance derived by Saffman (1965, 1968) for the lift experienced by a sphere in a slow ($Re < 1$) shear flow.

8.4. Comparison with numerical results

Due to the large computational power necessary to accurately resolve the wake behavior, numerical results are available only for cylinders but not for spheres. In Section 2.1 it was shown that the average lateral force should follow the same qualitative behavior for cylinders and spheres. However due to difference in the wake structure and, to a minor degree, in the stretching of vortex lines of the incoming fluid, the quantitative results should not be the same.

Therefore, numerical simulations are useful to identify relevant mechanisms, the force direction and how it changes with the Reynolds numbers. Jordan and Fromm (1972) calculated the force on a cylinder submerged in a weak shear flow at $Re = 400$. They found that the instantaneous lateral force oscillates in synchronization with the boundary layer separation point at both, the flow and high velocity side, and the average lift force was toward the low velocity side. Alajbegović et al. (1998) conducted numerical simulations for a fixed cylinder. The values of Re and Re_∇ belongs to the range used in the present work. These researchers found that the instantaneous lateral force oscillates around its average value and changes sign during each period. Moreover, the absolute value of the maximum instantaneous lift coefficients is much larger than that of the average coefficient.

9. Summary and conclusions

Rigid spheres attached to a tether were submerged in a turbulent uniform, downward, shear flow. As the tether interrupted two parallel beams, photo-transistors acquired the time sequence of beam interruptions, which was then sent to a PC for processing. From these data it was possible to determine the velocity and time fraction distributions. Two different methods were developed to measure time fractions as a function of position. The measurement methods require that the amplitude of the oscillations be large enough for both beams to be interrupted. Thus, the distance between beams is the main parameter determining the lowest Reynolds number, Re, for which the measurements can be conducted.

Time-averaged lateral forces were determined from the time fraction measurements through a static force balance among buoyancy, drag in the streamwise and lateral direction and lateral forces due to the mean shear. The methodology of the experiment is very similar to that of the two-fluid model since only average magnitudes of the flow are used to calculate the forces. This fact makes the results particularly suitable for application in two-fluid models. The error introduced by considering a static force balance and neglecting the average velocity and acceleration was estimated as three orders of magnitude smaller than the measured value.

Special attention was given to the lateral drag contribution in order to measure it as accurately as possible and to keep it small compared with the lateral forces produced by the mean shear. This work is the first in which lateral velocities in a turbulent uniform shear flow are reported. The slow decay of the uniform shear induce small lateral velocities. This in turn, makes it possible to have reliable measurements of the lateral forces due to the mean shear without a privileged direction for the lateral drag correction.

As expected from considerations of the kinetic energy of the turbulence in the wake, vortex shedding produces a lateral force opposite in direction to that of inviscid lift. The main non-dimensional parameter controlling the total lateral force was found to be the product of Reynolds numbers, $Re\,Re_\nabla$. At high values of $Re\,Re_\nabla$ wake effects dominate and the lateral force is toward the low velocity region. At smaller values of $Re\,Re_\nabla$ inviscid lift reverses the direction of the lateral force. These findings are quantified in Fig. 24. Evidence was found that the non-dimensional parameter $Re\,Re_\nabla$ is by itself insufficient to describe the behavior of the lift coefficient since the Reynolds number, Re, plays an important role too. This result was to be expected since Re is the main parameter determining wake structure.

Measurements of other researchers for $Re<300$ do not correlate with the product $Re\,Re_{\nabla}$. This fact is complementary evidence that only wake and inertia effects on the body, not the viscous contribution, are correlated by the parameter $Re\,Re_{\nabla}$. Significantly, the density of the sphere was found to have very little impact on lateral forces. This is an indication that small-amplitude, non-periodic pendant dynamics are similar to that of a fixed sphere.

Since the correlation developed in the present work, Eq. (41) is a local one, it should improve the accuracy and prediction capabilities of two-fluid models. In particular, it should help eliminate the need for fitting global lateral lift coefficients to experimental data, which limits a priori prediction capabilities.

The research presented herein not only provides a useful quantification of lateral forces in realistic conditions, but it also highlights the importance of vortex shedding instabilities in multiphase flows.

Acknowledgements

The financial support for this study by the ONR is gratefully acknowledged.

References

Alajbegović, A., 1994. Phase distribution and turbulence structure for solid/fluid upflow in a pipe. PhD thesis, Rensselaer Polytechnic Institute, Troy, New York.

Alajbegović, A., Assad, A., Bonetto, F., Lahey Jr., R.T., 1994. Phase distribution and turbulence structure for solid/fluid up flow in a pipe. Int. J. Multiphase Flow 20 (3), 453–479.

Alajbegović, A., Basara, B., Moraga, F.J., Bonetto, F.J., 1998. The lift force on a cylinder in a high Reynolds number shear flow. In: Int. Conf. Multiphase Flow. Paper No. 304. Lyon, France.

Aloui, F., Souhar, M., 1996a. Experimental study of a two-phase bubbly flow in a flat duct symmetric sudden expansion — Part I: visualization, pressure and void fraction. Int. J. Multiphase Flow 22 (4), 651–665.

Aloui, F., Souhar, M., 1996b. Experimental study of a two-phase bubbly flow in a flat duct symmetric sudden expansion — Part II: liquid and bubble velocities, bubble sizes. Int. J. Multiphase Flow 22 (5), 849–861.

Auton, T.R., 1987. The lift force on a spherical body in a rotational flow. J. Fluid Mech. 183, 199.

Auton, T.R., Hunt, J.C.R., Prud'Homme, M., 1988. The force exerted on a body in inviscid unsteady non-uniform rotational flow. J. Fluid Mech. 197, 241–257.

Batchelor, G.K., 1967. An Introduction to Fluid Dynamics. Cambridge University Press, Cambridge.

Bel Fdhila, R'Bei, 1991. Analyse expérimentale et modéelisation d'un écoulement vertical à bulles un élargissement brusque. PhD thesis, L'Institute National Polytechnique de Tolouse, Tolouse, France.

Borean, J.-L., Huilier, D., Burnage, H., 1995. Étude expérimentale d'une turbulence de grille à faible cisaillement. Comptes Rendues de'l Academie des Sciences 321 (Séries IIb), 19–24.

Blaker, J.W., 1971. Geometric Optics: The Matrix Theory. Marcel Dekker, New York.

Bretherton, F.P., 1962. Slow viscous motion round a cylinder in a simple shear. J. Fluid Mech. 12, 591.

Cherukat, P., McLaughlin, J.B., Graham, A.L., 1994. The inertial lift on a rigid sphere translating in a linear shear flow field. Int. J. Multiphase Flow 20 (2), 339–353.

Clift, R., Grace, J.R., Weber, M.E., 1978. Bubbles, Drops and Particles. Academic Press, New York.

Dandy, D.S., Dwyer, H.A., 1990. A sphere in shear flow at finite Reynolds number: effect of shear on particle lift, drag, and heat transfer. J. Fluid Mech. 216, 381–410.

Davies, J.M., 1949. The aerodynamics of golf balls. J. Appl. Phys. 20, 821–828.

Drew, D.A., Lahey Jr., R.T., 1987. The virtual mass and lift force on a sphere in rotating and straining inviscid flow. Int. J. Multiphase Flow 13 (1), 113–121.

Drew, D.A., Lahey Jr., R.T., 1990. Some supplemental analysis concerning the virtual mass and lift force on a sphere in a rotating and straining inviscid flow. Int. J. Multiphase Flow 16 (6), 1127–1130.

Eichhorn, R., Small, S., 1964. Experiments on the lift and drag on spheres suspended in a Poiseuielle flow. J. Fluid Mech. 20 (part 3), 513–527.

Elder, J.W., 1958. Steady flow through a non-uniform gauzes of arbitrary shape. J. Fluid Mech 5, 355–368.

Ervin, E.A., Tryggvason, G., 1994. The rise of bubbles in a vertical shear flow. In: Two Fluid Flows — With or Without Phase Change, AMD-184. ASME, New York.

Fan, L., Tsuchiya, K., 1990. Bubble wake dyanmics in liquid and liquid–solid suspensions. In: Butterworth-Heinemann Series in Chemical Engineering. Butterworth-Heinemann, London.

Ford, B., Loth, E., 1997. Forces on ellipsoidal bubbles in a turbulent shear layer. Private communication.

Grossetete, C., 1995. Caraterisation experimentale et simulations de l'evolution d'un ecoulement diphasique a bulles ascendant dans un conduite verticale. Collection de notes internes de la Direction des Études et Recherches. Electricité de France, December.

Jordan, S.K., Fromm, J.E., 1972. Laminar flow past a circle in shear flow. The Physics of Fluids 15 (6), 972–976.

Kariyasaki, A., 1987. Behavior of a single gas bubble in a liquid flow with a linear velocity profile. In: Proceedings of the 1987 ASME-JSME Thermal Engineering Joint Conference, 261–267.

Kelly, E., Wu, M., 1997. Path instabilities of rising air bubbles in a Hele–Shaw cell. Phys. Rev. Lett 79, 1265.

Kim, K.J., Durbin, P.A., 1988. Observations of the frequency in a sphere wake and drag increase by acoustic exitacion. Phys. Fluids 31, 3260–3265.

Lahey Jr., R.T., Lopez de Bertodano, M., Jones Jr., O.C., 1993. Phase distribution phenomena in complex geometry conduits. Nuclear Eng. and Design 141, 177–201.

Lance, M., Marié, J.L., Bataille, J., 1991. Homogeneous turbulence in bubbly flows. J. Fluids Eng. 113, 295.

Lighthill, J., 1986a. An Informal Introduction to Theoretical Fluid Mechanics. Oxford University Press, Oxford.

Lighthill, J., 1986b. Fundamentals concerning wave loading on offshore structures. J. Fluid Mech. 173, 667–681.

Lin, J.-C., Rockwell, D., 1996. Force identification by vorticity fields: techniques based on flow imaging. J. of Fluids and Structures 10, 663–668.

Lopez de Bertonado, M., 1991. Turbulent bubbly two-phase flow in a triangular duct. PhD thesis, Rensselaer Polytechnic Institute, Troy, New York.

Loth, E., Taeibi-Rahni, M., Tryggvason, G., 1997. Deformable bubbles in a free shear layer. Int. J. Multiphase Flow 23 (5), 977–1001.

Maccoll, J.W., 1928. Aerodynamics of a spinning sphere. J. Royal Aero 32, 777–798.

McCarthy, J.H., 1964. Steady flow past non-uniform wire grids. J. Fluid Mech. 19, 491–512.

Mei, R., 1992. An approximate expression for the shear lift force on a spherical particle at finite Reynolds number. Int. J. Multiphase Flow 18 (1), 145–147.

Moraga, F.J., Bonetto, F.J., Lahey, R.T., 1999. Periodic motion and body-wake lock-in of a rigid sphere in a turbulent uniform shear flow. In: Second Int. Symposium on Two-Phase Flow Modeling and Experimentation. Pisa, Italy.

Modi, V.J., Akutsu, T., 1984. Wall confinement effects for spheres in the Reynolds numbers range of 30–2000. Trans. ASME I: J. Fluids Engng. 106, 66–73.

Moraga, F.J., 1998. Lateral forces on rigid spheres in a turbulent uniform shear flow. PhD thesis, Rensselaer Polytechnic Institute, Troy, New York.

Naciri, A., 1992. Contribution à l'ètude des forces exercées par un liquide sur une bulle de gaz: portance, masse ajoutée et interactions hydrodynamique. PhD thesis, L'ecole Centrale de Lyon, Lyons, France.

Owen, P.R., Zienkiewicz, H.K., 1957. The production of uniform shear flow in a wind tunnel. J. Fluid Mech. 2 (Part 6), 521.

Rinne, A., Loth, R., 1995. Axial and radial development of local bubbly two-phase flow parameters for vertical bubbly flow in a pipe with sudden expansion. In: Celata, G.P., Shah, R.K. (Eds.), Two-Phase Flow Modelling and Experimentation. Edizioni ETS, Italy.

Rinne, A., Loth, R., 1996. Development of two-phase flow local parameters for vertical bubbly flow in a pipe with sudden expansion. Exp. Thermal and Fluid Science 13, 152–166.

Rose, W.G., 1966. Results of an attempt to generate a homogeneous turbulent shear flow. J. Fluid Mech. 25 (1), 97–120.

Rose, W.G., 1970. Interactions of grid turbulence with a uniform mean shear. J. Fluid Mech. 44 (4), 767–779.

Saleh, B.E.A., Teich, M.C., 1991. Introduction to Photonics. Wiley/Interscience, New York.

Saffman, P.G., 1956. On the rise of small air bubbles in water. J. Fluid Mech. 1, 249–275.

Saffman, P.G., 1965. The lift on a small sphere in a slow shear flow. J. Fluid Mech. 22, 385.

Saffman, P.G., 1968. Corrigendum to The lift on a small sphere in a slow shear flow. J. Fluid Mech. 31, 624.

Sarpkaya, T., 1979. Vortex-induced oscillations: a selective review. J. Applied Mechanics 46, 241.

Sakamoto, H., Haniu, H., 1990. A study on vortex shedding from spheres in an uniform flow. J. Fluids Eng. 112, 386–392.

Sakamoto, H., Haniu, H., 1995. The formation mechanism and shedding frequency of vortices from a sphere in uniform shear flow. J. Fluid Mech. 287, 151–171.

Serizawa, A., Kataoka, I., 1987. Phase distribution in two phase flow. In: ICHMT Int. Seminar on Transient Phenomena in Multiphase Flow. Dubrovnik, Yugoslavia, 179–224.

Sridhar, G., Katz, J., 1995. Drag and lift forces on microscopic bubbles entrained by a vortex. Phys. Fluids 7 (2), 389–399.

Stansby, P.K., 1976. The locking-on of vortex shedding due to the cross-stream vibration of circular cylinders in uniform and shear flows. J. Fluid Mech. 74 (part 4), 641–665.

Tagaki, S., Matsumoto, Y., 1995. Three dimensional calculation of a rising bubble. In: Proceedings of the 2nd. Int. Conf. on Multiphase Flow. Kyoto, Japan, PD2-9–PD2-16.

Taeibi-Rahni, M., Loth, E., 1996. Forces on a large cylindrical bubble in an unsteady rotational flow. AIChe J. 42 (3), 638.

Taneda, S., 1957. Negative Magnus effect. Rep. Res. Inst. Appl. Phys. (Kyushu) 20, 123–128.

Tomiyama, A., Žun, I., Sou, A., Sakaguchi, T., 1993. Numerical analysis of bubble motion with the VOF method. J. Nuclear Eng. and Design 141, 69–82.

Tomiyama, A., Sou, A., Žun, I., Kanami, N., Sakaguchi, T., 1995. Effect of Eotvos number and dimensionless liquid volumetric flow on lateral motion of a bubble in a laminar duct flow. In: Proceedings of the 2nd. Int. Conf. on Multiphase Flow. Kyoto, Japan, PD1-11–PD1-18.

Torobin, L.B., Gauvin, W.H., 1960. Fundamental aspects of solid–gas flow-V: the effect of fluid turbulence on the particle drag coefficient. Can. J. Mech. Eng. 38, 142–153.

Viets, H., 1971. Accelerating sphere-wake interaction. AIAAA J. 9, 2087–2089.

Yamamoto, F., Koukawa, M., Monya, H., Teranishi, A., Miyamoto, H., 1993. An experimental study for simulation of pneumatic conveying (lift and drag applied to a sphere in high Reynolds-numbers linear shear flows). Int. J. JSME 36 (2), 294–299.

Yamamoto, F., Ohta, J., Iguchi, M., Kawamoto, T., 1995. Experiments and numerical simulation on particle motion in the linear shear flow. In: Proc. 2nd. Int. Conf. Multiphase Flow, Kyoto, Japan, PD2-35–PD2-42.

Wang, S.K., Lee, S.J., Jones Jr., O.C., Lahey Jr., R.T., 1986. 3-D turbulence structure and phase distribution measurements in bubbly two-phase flows. Int. J. Multiphase Flow 13 (3), 327–343.

Wang, S.K., 1986. Three-dimensional turbulence structure measurements in air/water two-phase flow. PhD thesis, Rensselaer Polytechnic Institute, Troy, New York.

Žun, I., 1985. The role of void peaking in vertical two-phase bubbly flow. In: Proc. of the 2nd Int. Conf. on Multiphase Flow, London, England, 127–139.